

# JGR Atmospheres

## RESEARCH ARTICLE

10.1029/2022JD037469

### Key Points:

- Mid-latitude synoptic fronts leave a distinct isotope signature in the Alpine snow cover that is preserved during the cold season
- The cloud formation temperature determines the  $\delta^{18}\text{O}$  and  $\delta\text{D}$  of the buried snow, and moisture source information is preserved in the deuterium excess
- Post-depositional dry metamorphism acts to smooth the snow isotope profile, while wet snow metamorphism leads to an enrichment of the snow

### Supporting Information:

Supporting Information may be found in the online version of this article.

### Correspondence to:

F. Aemisegger,  
[franziska.aemisegger@env.ethz.ch](mailto:franziska.aemisegger@env.ethz.ch)

### Citation:

Aemisegger, F., Trachsel, J., Sadowski, Y., Eichler, A., Lehning, M., Avak, S., & Schneebeli, M. (2022). Fingerprints of frontal passages and post-depositional effects in the stable water isotope signal of seasonal Alpine snow. *Journal of Geophysical Research: Atmospheres*, 127, e2022JD037469. <https://doi.org/10.1029/2022JD037469>

Received 14 JUL 2022

Accepted 7 OCT 2022

### Author Contributions:

**Conceptualization:** F. Aemisegger, J.

Trachsel, A. Eichler, M. Schneebeli

**Formal analysis:** F. Aemisegger

**Funding acquisition:** A. Eichler, M. Schneebeli

**Investigation:** J. Trachsel, A. Eichler, S. Avak

**Methodology:** F. Aemisegger, Y. Sadowski, A. Eichler, M. Lehning



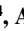




**Visualization:** F. Aemisegger

**Writing – original draft:** F. Aemisegger, J. Trachsel

**Writing – review & editing:** J. Trachsel, Y. Sadowski, A. Eichler, M. Lehning, S. Avak, M. Schneebeli

© 2022. American Geophysical Union.  
All Rights Reserved.

## Fingerprints of Frontal Passages and Post-Depositional Effects in the Stable Water Isotope Signal of Seasonal Alpine Snow

F. Aemisegger<sup>1</sup> , J. Trachsel<sup>2,3</sup> , Y. Sadowski<sup>2,4</sup> , A. Eichler<sup>5,6</sup> , M. Lehning<sup>2,4</sup> , S. Avak<sup>5,6,7</sup> , and M. Schneebeli<sup>2</sup> 

<sup>1</sup>Institute for Atmospheric and Climate Science, ETH Zurich, Zurich, Switzerland, <sup>2</sup>WSL-Institute for Snow and Avalanche Research SLF, Davos Dorf, Switzerland, <sup>3</sup>Department of Environmental Systems Science, ETH Zurich, Zurich, Switzerland, <sup>4</sup>School of Architecture, Civil and Environmental Engineering, École Polytechnique Fédérale de Lausanne (EPFL), Lausanne, Switzerland, <sup>5</sup>Laboratory of Environmental Chemistry, Paul Scherrer Institute, Villigen, Switzerland, <sup>6</sup>Oeschger Centre for Climate Change Research, University of Bern, Bern, Switzerland, <sup>7</sup>Department of Chemistry and Biochemistry, University of Bern, Bern, Switzerland

**Abstract** Stable water isotopes are used as a paleothermometer in ice cores for climate reconstructions over the past millennia. The underlying physical processes involved in the isotope-temperature relation, however, unfold at much shorter timescales. Here, we study the temporary archival of frontal passages in the seasonal Alpine snow cover. We combine five snow profiles sampled in winter 2017 at the Weissfluhjoch with a quantitative snow layer age reconstruction and atmospheric reanalysis data to characterize the circulation and clouds associated with the precipitation producing synoptic-scale cold and warm fronts. We find that the vertical cloud structure and the air parcels' net cooling during transport leave a distinct imprint in the  $\delta^{18}\text{O}$  and  $\delta\text{D}$  vertical profile in the snow. The near-surface humidity gradient at the moisture source is reflected in the second order isotope parameter deuterium excess. In the cold season, these environmental conditions during cloud formation and at the moisture source are preserved in the snow. In the melt season, significant post-depositional effects due to wet snow metamorphism, however, leads to an enrichment in heavy isotopes in the snow and a strong smoothing of the initial atmospheric imprint. These findings show that the isotope signal archived in the dry snow cover is strongly modulated by individual weather systems prior to deposition. Major shifts in the upper-level jet stream and cyclone tracks likely leading to changes in moisture source regions and conditions, could therefore be detectable in the isotope composition of Alpine ice.

**Plain Language Summary** To obtain information on past climate conditions, the non-radioactive, heavy versions of the water molecule are often used as paleothermometers in ice cores. However, the processes that determine how this paleothermometer works, act at the weather-system timescale (days), not the climate timescale (years). In this paper, we illustrate how isotope information from five snow profiles relate to the history of the water in the atmosphere during frontal passages. We show that the meteorological conditions at the evaporative source and in the clouds where the snow crystals are formed, determine the concentration of stable water isotopes in the snow. Transformation processes of the snow's structure, after it has been deposited do not significantly alter the isotope signals in the cold season. However, as soon as melting starts, the heavy water molecules accumulate in the snow, while the lighter ones are washed out.

## 1. Introduction

The oxygen and hydrogen isotope composition of snow and ice is widely used to reconstruct past temperature conditions (Craig, 1961; Cuffey et al., 1995; Dansgaard, 1964; Eichler et al., 2009; Johnsen et al., 1995; Masson-Delmotte et al., 2005; Steig et al., 2013; Thompson et al., 2013). The physical basis for linking the isotope signals in the ice with past temperatures is given by the temperature-dependence of the saturation vapor pressure of water and its isotopologues (Clausius-Clapeyron relation) established based on monthly precipitation data (Dansgaard, 1953; Epstein & Mayeda, 1953). Temperature reconstructions from ice cores often cover timescales of several millennia with temporal resolutions of between a month and a decade, depending on the resolution of the analysis technique applied (Gkinis et al., 2021; Jouzel, 2013; Mariani et al., 2014). The intrinsic timescale of the process-based link between the isotope signals buried in the snow and the relevant atmospheric conditions is, however, much shorter (on the order of hours–days). In this paper, we explore the latter link using isotope signals from snow profiles measured at the Weissfluhjoch in Switzerland combined with diagnostics

based on atmospheric reanalysis data. We aim to provide the basic understanding needed for leveraging meteorological information from snow cores at remote locations without meteorological instrumentation, and for extracting information about shifts in atmospheric circulation patterns from ice cores.

The abundance of the heavy isotopologues (hereafter named isotope)  $\text{D}^1\text{H}^{16}\text{O}$  and  $^1\text{H}_2^{18}\text{O}$  is expressed by the  $\delta$  notation ( $\delta\text{D}$  and  $\delta^{18}\text{O}$ , respectively, Dansgaard (1964)), which is defined as the isotopic ratio  $R$  of the concentration of the heavy isotope to the concentration of the light isotope  $^1\text{H}_2^{16}\text{O}$  normalized with an internationally accepted standard isotopic ratio (the Vienna Standard Mean Ocean Water, VSMOW2, Coplen (2011); IAEA (2017); with  $^2R_{\text{VSMOW2}} = 1.5576 \cdot 10^{-4}$  and  $^{18}R_{\text{VSMOW2}} = 2.0052 \cdot 10^{-3}$ ):  $\delta^{18}\text{O} = \left( \frac{^{18}R_{\text{sample}}}{^{18}R_{\text{VSMOW2}}} - 1 \right)$  and  $\delta\text{D} = \left( \frac{^2R_{\text{sample}}}{^2R_{\text{VSMOW2}}} - 1 \right)$ .

In the following, two sections we shortly review the relevant physical processes in the atmosphere (Section 1.1) and the snow (Section 1.2), which impact the isotope composition of the snow cover. The aims of this study are presented in Section 1.3.

### 1.1. Atmospheric Processes

When following the water vapor in an air parcel from its evaporative moisture source to the precipitation sink, several phase change processes can affect its isotope composition. Phase change processes are associated with so-called isotopic fractionation effects (see, e.g., Gat (1996)). Ocean evaporation is a process during which heavy water molecules preferentially stay in the liquid phase due to their stronger hydrogen bonds (equilibrium fractionation effect) and smaller diffusivities through an unsaturated laminar layer (non-equilibrium fractionation effect). These isotope fractionation processes are dependent on the thermodynamic conditions of the environment during the phase change, which are  $T_s$ , the surface temperature and  $h_s$ , the relative humidity normalized to  $T_s$  (Craig & Gordon, 1964). The isotope ratio of the freshly formed water vapor  $R_{\text{sample}}$  is thus lower than the isotope ratio of ocean water (usually very close to  $R_{\text{VSMOW2}}$ ) with resulting  $\delta$ -values of atmospheric waters that are mostly negative.

During cloud formation, the condensation temperature and the level of supersaturation determine the isotope composition of the condensate. Some of these clouds can form precipitation, leading to preferential removal of heavy isotopologues, along with a moist adiabatic cooling of the air parcel forming the cloud (e.g., Dansgaard, 1964; Dütsch et al., 2017). Typically, when clouds and precipitation formation are associated with synoptic-scale weather systems, large-scale convergence is involved, and therefore air parcels from different origin and with different histories contribute to the precipitation. The combination of processes at the moisture source, during transport and cloud formation at the site of the ice core therefore results in a complex relation between the  $\delta\text{D}$  and  $\delta^{18}\text{O}$  composition of the water vapor in the air and its temperature (Jouzel et al., 1997). The second-order isotope variable deuterium excess  $d = \delta\text{D} - 8 \cdot \delta^{18}\text{O}$  (Dansgaard, 1964) is a measure for the strength of non-equilibrium fractionation and is a particularly interesting tracer for moisture source conditions (Aemisegger & Sjolte, 2018; Pfahl & Wernli, 2008).

Since all the above mentioned processes involved in the atmospheric water cycle are inherently linked to temperature (Craig, 1961; Dansgaard, 1964), the resulting empirical relations between the  $\delta\text{D}$  and  $\delta^{18}\text{O}$  of precipitation and local surface temperature are often found to be very strong at annual or interannual timescales (Dansgaard, 1964; Jouzel et al., 1997; Masson-Delmotte et al., 2008). However, at some sites such as the high-Alpine Grenzgletscher high-accumulation site (Eichler et al., 2000, 2001), the correlation between the  $\delta^{18}\text{O}$  signal in the ice core and annual mean temperature from the nearby meteorological stations is low (Mariani et al., 2014). Brönnimann et al. (2013) showed that much better correlations between the  $\delta^{18}\text{O}$  signal and annual precipitation-weighted mean temperatures can be obtained than between  $\delta^{18}\text{O}$  and the annual mean site temperature. Similar conclusions have been drawn in other studies based on polar ice cores (Laepplé et al., 2011; Sime et al., 2009; Werner et al., 2000).

### 1.2. Snow Processes

In addition to precipitation intermittency, other factors can modulate the relation between the air temperature and the isotope signal recorded in the snow (Beria et al., 2018; Casado et al., 2018; Sturm et al., 2010). Post-depositional processes such as blowing and drifting snow, diffusion within the snow cover, surface melting, and sublimation

lead to a smoothing of the signal within the ice core (Eichler et al., 2001). Stichler et al. (2001) have isolated sublimation at the surface of the snow cover and diffusive mixing of water vapor within the firn as the main processes for altering the isotopic record in high-altitude glaciers. Bohleber et al. (2013) have shown an increase in the mean isotopic signal at a low-accumulation high-altitude site (Colle Gnifetti), where a substantial fraction of the isotopically depleted winter precipitation is lost by wind erosion. Furthermore, changes in the surface snow isotope composition have been linked to exchange with ambient water vapor due to sublimation-desublimation cycles over the Greenland ice sheet (Madsen et al., 2019; Steen-Larsen et al., 2014) and in Antarctica (Casado et al., 2018). Within the snow cover, snow metamorphism (Ebner et al., 2017) and water flow during melt or rain events (Lee et al., 2009) can affect the isotopic signal.

From a mechanistic point of view, snow metamorphism, which describes the recrystallization that snow undergoes after deposition, is the key post-depositional process in addition to self-weight settling responsible for the rapid compaction of new snow and the resulting smoothing of the isotope signal in the snow interior. In the following, the relevant fractionation processes associated with wet and dry snow metamorphism are shortly summarized:

- *Dry snow metamorphism* describes the recrystallization that snow undergoes after deposition, as long as no meltwater is present. Crystal surfaces with a higher equilibrium vapor pressure at warmer or more convex locations sublime, while at colder or concave places vapor deposition occurs (Pinzer et al., 2012; Sokratov & Maeno, 1997). The latter local rearrangements can completely renew high-alpine snowpacks at the surface and thereby transform the structure of the original ice crystals (Pinzer et al., 2012). How this complete rearrangement of the snowpack affects the isotope signal in detail is not yet clear (Ebner et al., 2017; Sturm & Benson, 1997).
- As soon as liquid water is present in the snow cover, the process of *wet snow metamorphism* is initiated. The snowpack can reach the melting point due to incoming shortwave radiation close to the surface, by heat diffusion or when liquid water flows through it. In contrast to other porous media, for example, as in soils, the liquid water in the snow cover leads to a coarsening of the snow structure (Colbeck, 1986; Raymond & Tusima, 1979). The large particles grow at the expense of the smaller particles, whereby the melted mass is deposited on the larger structures (Albert & Krajewski, 1998). The growth rate is strongly dependent on the liquid water content (LWC) (Avanzi et al., 2017; Brun, 1988) and is many times faster than during dry metamorphism. Denoth (1982) introduced two idealized states summarizing the effect of meltwater on the snow cover depending on the infiltration rate. State (a) is the “pendular system” with low flow rates, in which the capillary tension is high enough to retain most of the meltwater penetrating from the surface into the snow cover. In this state, the water of the dissolved crystals is available for crystal growth. Thus the bulk isotope composition of the snow cover is not altered, even though fractionation processes take place both during melting and freezing. State (b) is the “funicular system,” in which higher flow rates occur due to the higher liquid water contents, for which the capillary flow is overcome by gravitational flow (Walter et al., 2013). In this case, the bulk concentration is changed due to the meltwater runoff. The transition between the two states is very sensitive to the structure of snow; it decreases from approximately 13%–18% liquid saturation for new snow to 7%–12% saturation for old, coarse-grained snow (Denoth, 1982). Snowmelt preferentially discharges isotopically light water, thereby enriching the residual snowpack in heavy isotopes (e.g., Albert and Hardy, 1995; Taylor et al., 2001). The contribution of wet snow metamorphism to the change in the isotope signal during the melting period is likely key in the widely observed “melt-out effect” of the snow cover (Ala-Aho et al., 2017), that is, the progressive enrichment of both the snow cover and the meltwater as the melt season progresses.

### 1.3. Isotope Meteorology in Snow

Due to the complexity of the atmospheric processes involved in moisture transport, cloud formation, precipitation, and the post-depositional processes at play, including snow metamorphism, the question arises, if the environmental conditions associated with individual weather events leading to significant snow accumulation at a given site, can be recorded in the snow cover (Dansgaard, 1953, 1964). So far, this sequence of processes including both pre- and post-depositional effects has rarely been investigated as a whole, especially not in alpine and polar regions with high accumulation. Thus, combining our expertise in atmospheric dynamics and snow physics

we aim at improving our understanding of this process-chain and propose to study the archival of atmospheric information in snow at the synoptic timescale in the Alps.

Baltensperger et al. (1993) found a good agreement between the measured  $\delta^{18}\text{O}$  in new snow and samples derived from a snow pit at the beginning of spring at the Weissfluhjoch site (WFJ) in the Swiss Alps. However, from the latter study, it remains unclear how short-term changes in the isotope signal of the precipitation during frontal precipitation events are transferred into the snow cover. Our study is based on five high-resolution profiles sampled approximately every month at the WFJ, a Swiss Alpine measurement site (2,536 m a.s.l.). We combined the stable water isotope signal from these profiles with a model-based snow layer age reconstruction and ERA5 atmospheric reanalysis data from the European Centre for Medium-Range Weather Forecasts (ECMWF) for assessing the atmospheric moisture source, transport and cloud formation conditions using air parcel-based and frontal cloud-characterizing diagnostics.

The three research questions, which we address with this study, are:

1. What is the impact of post-depositional dry and wet snow metamorphism on the isotope profiles? (Section 3)
2. Despite these post-depositional effects, can we establish a solid link between the buried snow isotope signal and the diagnosed atmospheric conditions, that is, the local cloud formation temperature and moisture source conditions? (Section 4)
3. Can frontal passages with significant accumulation be detected in the snow profiles and are they associated with characteristic isotope signals? (Section 5)

Based on our findings related to these research questions, we envision three main applications, which are: (a) obtain meteorological information of a given cold season from a single isotope profile in snow or firn in remote locations without meteorological instrumentation, as well as from pre-instrumental time periods, (b) obtain frequencies of precipitation input from warm/cold air masses from snow or firn cores, from the Alps, the Himalayas, the Andes, Svalbard or Greenland, (c) reconstructing the storm track dynamics (inter-annual variations in the frequency of occurrence of extratropical cyclones) from multiple ice core sites (Aemisegger, 2018).

Before we address our research questions in the results Sections 3–5 and in the above order, the experimental and modeling methods are described in Section 2. Finally, we draw conclusions in Section 6.

## 2. Experimental and Modeling Methods

The following three sub-sections summarize the experimental and modeling approaches chosen for investigating the importance of snow metamorphism and atmospheric processes on the stable water isotope composition of the snow in winter 2016/2017 at the WFJ site in the Swiss Alps. Sections 2.1 and 2.2 describe the stable water isotope sampling and analysis procedure. Section 2.3 introduces the modeling framework used for reconstructing the age of the snow layers, which allows us to link the isotope signals in the snow with atmospheric processes. Section 2.4 summarizes the combination of data sets and diagnostics used for the meteorological analysis of the snowfall events.

### 2.1. Snow Profile Sampling

The WFJ measurement site of the Institute for Snow and Avalanche Research is located above Davos at 2,536 m above sea level (46°49′47″N 9°48′33″E). The site is a reference CryoNet station (Marty & Meister, 2012). In winter 2017, the campaign to monitor the isotope signal in the snowpack took place from January to June (Figures 1a and 1b). In parallel to the isotope profile sampling campaign, an extensive measurement program to characterize the snow cover at the WFJ site took place (Calonne et al., 2020).

The snow sampling procedure is described in detail in Avak et al. (2019a) and Avak et al. (2019b), which focuses on the chemical results of the sampled profiles, based on trace element and major ion analysis. Here, we shortly summarize the most important sampling steps. The isotope samples of the entire snow pit were collected on 25 January, 22 February, 21 March, 17 April, and 1 June with a vertical resolution of 6 cm, corresponding to 2 and 3 cm in snow water equivalent (SWE), depending on the snow density. Snow depths during sampling varied between 185 cm (21 March) and 83 cm (1 June). Earlier studies conducted at the WFJ site by Baltensperger et al. (1993) and Schwikowski (1997) point to a uniform snow deposition over the field site. Nevertheless, topog-

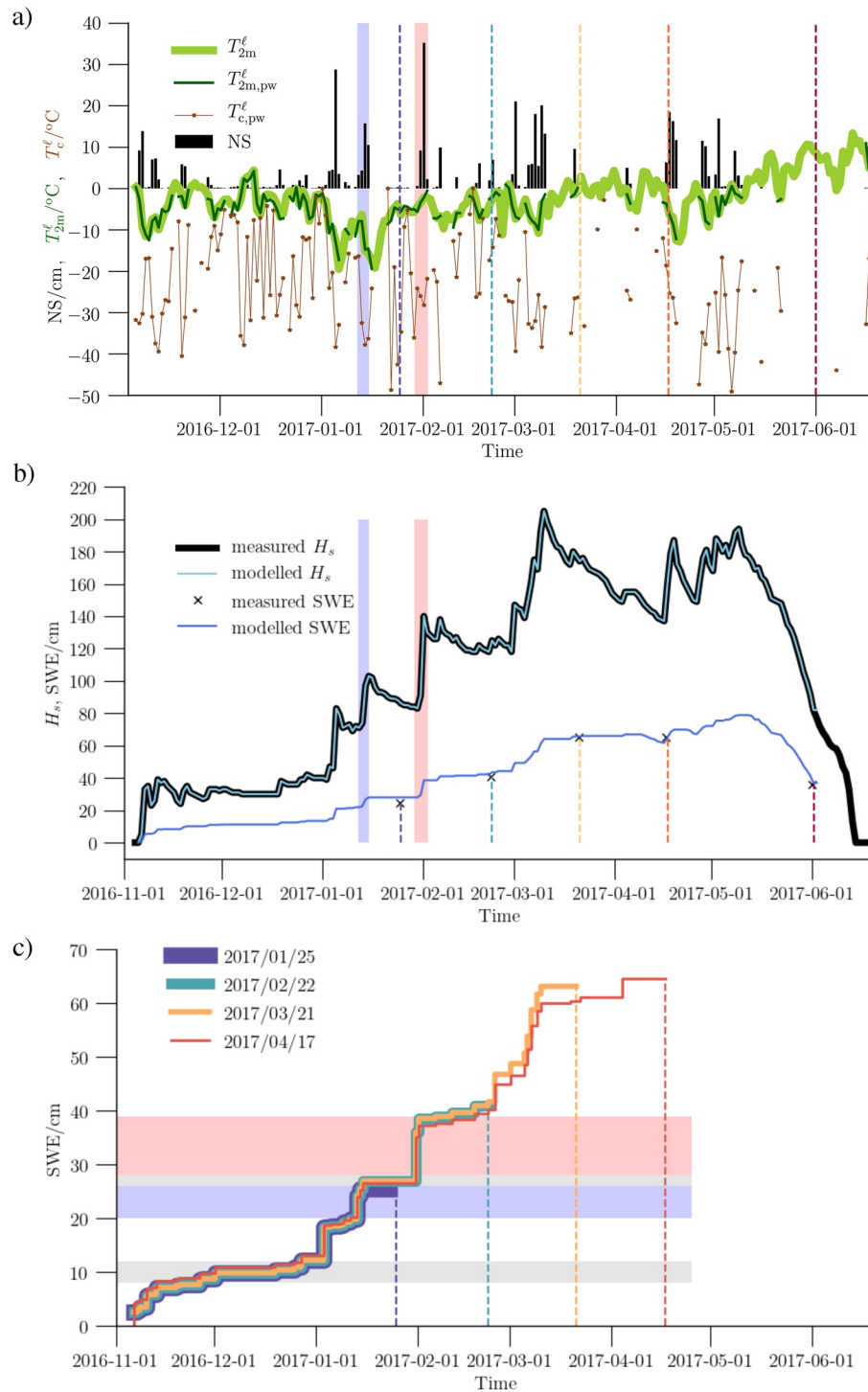


**Figure 1.** Time series of the winter 2016–2017 (a) daily meteorological conditions and (b and c) the snow cover evolution at Weissfluhjoch. In (a) new snow (NS) is shown by black bars, daily means of 2 m air temperature ( $T_{2m}^e$ ) by the thick light green line, daily precipitation weighted mean 2 m air temperature ( $T_{2m,pw}^e$ ) by the thin dark green line, the cloud formation temperature by the thin brown dots and line ( $T_{c,pw}^e$ , precipitation weighted). In (b) the measured snow height and snow water equivalent (SWE) are shown in black (line and crosses, respectively), the  $\Delta$ snow modeled snow height in light blue and SWE in royal blue. In (c) the age reconstruction obtained from  $\Delta$ snow is shown for the four profiles that were taken before the start of the melt season. The June profile is strongly affected by melting, which makes the age reconstruction with  $\Delta$ snow unreliable. The age reconstruction for the June profile is therefore not shown in (c). In all panels the timing of the sampling of the five profiles is indicated by dashed lines and the passage of the studied cold and warm fronts (discussed in Section 5) is highlighted by blue and red shading. Gray shading in (c) indicates prolonged periods with very low accumulation.



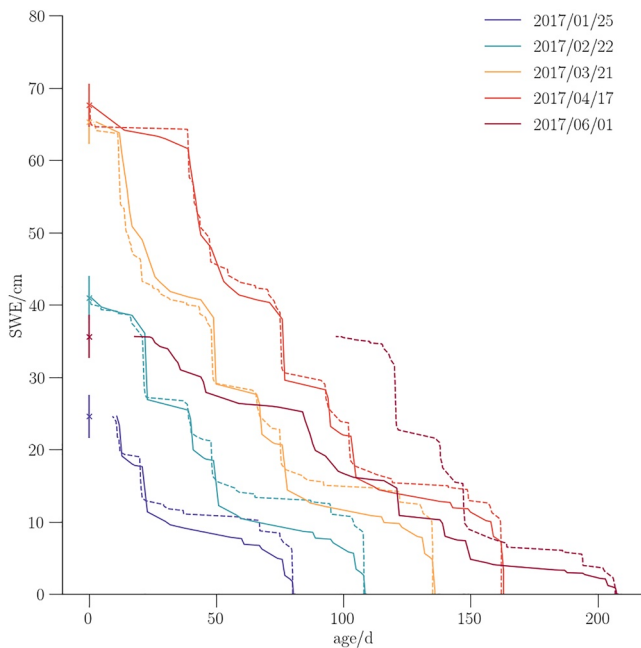


**Figure 2.** Age reconstruction by  $\Delta$ snow (solid lines) and SNOWPACK (dashed lines) for the dates of the five sampled profiles from Weissfluhjoch. The measured snow water equivalent (SWE) on the day of the profile sampling is shown by a cross including an errorbar indicating the sampling uncertainty. The age is measured in number of days before sampling of a given profile at age = 0.

raphy, preferential deposition (Lehning et al., 2008) and snow transport are known to vary across the site (Doorschot et al., 2004) and affect the analysis as shown in Section 2.3, since the position of the individual snow profiles were up to 20 m apart. The sampling was carried out starting from the surface to the ground. For this purpose, a rectangular (15 × 24 cm) polycarbonate sampler was inserted horizontally into the profile wall. Then 50 ml polypropylene containers (Sarstedt, Nümbrecht, Germany) were pushed downwards toward the sampler. The samples were hermetically sealed and transported in frozen state to the laboratory of the Paul Scherrer Institute (PSI).

## 2.2. Isotope Analysis

The frozen samples were melted at room temperature and analyzed for stable water isotopes at the PSI (Avak et al., 2019a; Avak et al., 2019b). For the determination of  $\delta D$  and  $\delta^{18}O$ , 1 ml aliquots were used. A wavelength-scanned cavity ring down spectrometer (WS-CRDS, L2130-i Analyzer, Picarro, Santa Clara, CA, USA) at PSI was used for the analysis. The samples were injected into a vapourizer (A0211, Picarro, Santa Clara, CA, USA) using PAL HTC-xt autosampler (LEAP Technologies, Carrboro, NC, USA). Every sample was injected 6 times and the first three injections discarded to account for memory effects. Three internal standards were measured after every tenth sample to calibrate and monitor instrumental drifts. The uncertainty of the measurement is 0.1‰ for  $\delta^{18}O$  and 0.5‰ for  $\delta D$ .

## 2.3. Tracking Snow Layer Age

A quantitative age reconstruction of the sampled 6 cm snow layers was performed using two different snow models (Figure 2): the semi-empirical

$\Delta$ snow model (Winkler et al., 2021b) and the thermodynamic SNOWPACK model (Bartelt & Lehning, 2002; Lehning et al., 2002; Lehning et al., 2002a).

$\Delta$ snow was originally designed to model snow water equivalents (SWE) solely based on daily snow height measurements (Marty & Meister, 2012), which makes this multi-layer snow model attractive to use at remote locations, where only snow height measurements are available (e.g., from remote sensing).  $\Delta$ snow takes into account the key processes of snowpack transformation by dry and wet metamorphism, as well as deformation. It neglects the effects of snow drift, sublimation, and rain on snow.  $\Delta$ snow follows the rules of Newtonian viscosity to represent compaction (dry metamorphism and deformation), and models overburden loads due to new snow as additional compaction (Winkler et al., 2021b). A new snow event generates a new snow layer with a density of  $\rho_0 = 100 \text{ kg m}^{-3}$  (assumed to be constant over the winter) at the top of the snow cover and is detected by an increase in measured snow height of more than a given threshold of measurement uncertainty ( $\tau = 2 \text{ cm}$ ). When snow melt occurs, the water mass is distributed from top to bottom in the snowpack. If all modeled snow layers reach the maximum density of  $\rho_{\text{max}} = 450 \text{ kg m}^{-3}$  the runoff produced is distributed over all snow layers, thus leading to a thinning of all layers but not reducing the number of layers. The seven  $\Delta$ snow model parameters were calibrated using the five measured SWE values on the profiling days within the suggested physically meaningful ranges proposed in Winkler et al. (2021b) (see Supporting Information S1 for more details on parameter setting).

To evaluate the age reconstruction by  $\Delta$ snow in an independent way, the more complex thermodynamic SNOWPACK model was used. SNOWPACK explicitly represents the mass and energy exchanges within the ground-snow-atmosphere continuum. Compared to  $\Delta$ snow, SNOWPACK therefore represents the snow cover in a more detailed way and takes into account processes such as sublimation, rain on snow, and a realistic water transport scheme (Wever et al., 2014), albeit without drifting snow module. Due to its higher complexity, SNOWPACK also requires more observations for driving the model. The simulation used in this study was driven by half-hourly meteorological and snowpack measurements from the automatic weather station at the WFJ site (Marty & Meister, 2012). The snow heights from the automatic ultrasound sensor with half-hourly resolution are affected by spurious snow height changes and show large deviations from the more precise daily manual snow

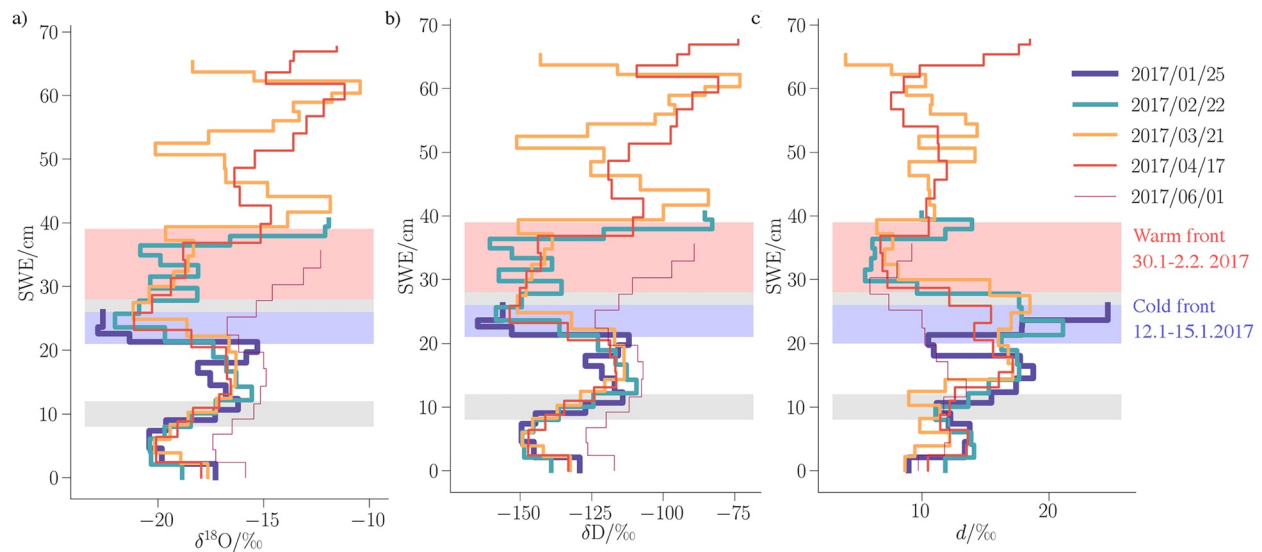


**Figure 3.** Five profiles sampled at the Weissfluhjoch between January and June 2017 of  $\delta^{18}\text{O}$  (a),  $\delta\text{D}$  (b),  $d$  (c) as a function of snow water equivalent (SWE). Blue, red and gray shadings as in Figure 1.

height measurements. The automatic snow height data was therefore corrected to match the manual observations (see Supporting Information S1 for more information on this correction). The density of new snow is variable in time in SNOWPACK and determined using an empirical relation between meteorological variables and snow density measurements (Schmucki et al., 2014). The snowpack is considered to be a linear viscoelastic material, with settlement calculated as described in Lehning et al. (2002a). Liquid water flow in snow is solved using the Richards equation as recently implemented by Wever et al. (2014). Rainfall on snow is accounted for and rainfall intensity data is used whenever the air temperature exceeds 1.2°C (see Schmucki et al. (2014)). The surface sensible and latent heat flux parameterizations are derived from Monin-Obukhov similarity (Lehning et al., 2002).

For the age reconstruction of the sampled snow layers in the five profiles using  $\Delta\text{snow}$  and SNOWPACK, the measured SWE of the samples is taken as a reference. SWE is chosen as a vertical snow coordinate, because it is conserved during compaction and therefore allows a direct comparison of the five sampled profiles' isotope composition (e.g., in Figures 3 and 6). A nearest neighbor search was applied for matching observed SWEs with modeled layer SWEs including a SWE search window of 1.6 cm to take into account measurement uncertainties. The age reconstruction is performed from top-down to achieve the best possible reconstruction of the most recent layers accumulated just before the respective profile sampling dates. The interpolation of measured SWE depths (top-down) or heights (bottom-up) leads to similar layer age, with slight shifts of on average 2 cm due to the different reference level.

The obtained age reconstruction of the five sampled profiles with  $\Delta\text{snow}$  and SNOWPACK are consistent for the cold part of the winter, without significant impact of snow melt (Figure 2). Somewhat larger deviations between the two reconstructions are found for the prolonged period without significant accumulation in December 2016 (Figure 2 at ~12 cm SWE). For the last profile in June, when the snow cover contained large amounts of LWC (See Figure S3 in Supporting Information S1) the two age reconstructions strongly differ, due to the different treatments of wet metamorphism and runoff formation. SNOWPACK shows a more realistic behavior than  $\Delta\text{snow}$  due to its explicit representation of the LWC in snow. SNOWPACK first melts the top layers, while  $\Delta\text{snow}$  produces melt water from all layers that exceed the maximum density, thereby keeping the layer structure and removing mass from the whole snow cover. This explains the much larger snow layer age estimates obtained from  $\Delta\text{snow}$  compared to the layer age simulated by SNOWPACK.

To validate and further compare the SNOWPACK and  $\Delta\text{snow}$  simulations, Table 1 summarizes the root mean square difference (RMSD) and mean bias between the measured and the simulated snow cover height  $H$  and SWE. A large share of the mismatch between observed values at the sampling location and the simulated values originate from differences between the observational data set driving the simulations (i.e., the snow height observation at the reference location of the site) and the profile location. Small inhomogeneities of the underlying

**Table 1**

Root Mean Square Difference (RMSD), Range of Bias, and Mean Bias of Total Snow Cover Snow Water Equivalent (SWE) and  $H$  Simulated by  $\Delta$ Snow and SNOWPACK With Respect to the Five Sampled Snow Profiles

Data set	RMSD/cm	Range of bias/cm	mean bias/cm
$H_{s,ref}$ , $\Delta$ snow $H$	5.6	−11 to −1	−4.0
$\Delta$ snow SWE	2.4	−2.5 to +3.3	+1.0
SNOWPACK $H$	7.9	−11.8 to −0.6	−4.68
SNOWPACK SWE	5	−6.6 to 3.2	−2.8

Note.  $H_{s,ref}$  is the daily reference measurement at maximum 20 m from the location of the sampled profile.

topography, slight variations of the snow cover surface due to wind drift, and measurement uncertainties lead to measured  $H$  at the location of the profiling that are on average 4 cm higher than the  $H$  measured at the reference location (Table 1). This highlights the importance of high-quality snow height observations for precise snow layer age reconstruction. The snow height observations should match as closely as possible with the snow cover dynamics of the profiling location.

#### 2.4. Meteorological Characterization of Snowfall Events

For the meteorological characterization hourly data is used from the WFJ station and from the ERA5 reanalysis data set (C3S—Copernicus Climate Change Service, 2017; Hersbach et al., 2019, 2020) of the ECMWF. Local observations of 2 m air temperature (ventilated) as well as the corrected automatic snow height measurements are used from the WFJ station. The ERA5 data is used to diagnose different properties of precipitation producing clouds at the WFJ and to identify moisture sources and the conditions during evaporation and transport based on three-dimensional backward trajectories.

Seventy to 80% of winter and spring precipitation at the WFJ occurs due to frontal passages, while the share of precipitation induced by local convective systems is very low (Rüdisühli et al., 2020). Frontal passages have been shown to strongly modulate the isotope composition of midlatitude precipitation (Aemisegger et al., 2015; Dansgaard, 1953; Weng et al., 2021). The synoptic-scale nature of the precipitation events leading to accumulation of snow at the WFJ in winter and spring, warrants the use of the ERA5 reanalysis data for the meteorological characterization. ERA5 likely reproduces the key dynamical features of the precipitation generating systems, such as their moisture origin, transport conditions, large-scale cloud properties (vertical and horizontal extent, approximate level of hydrometeor formation) and precipitation timing.

The hourly properties of precipitating clouds such as cloud formation temperature ( $T_c^\ell$ ) and cloud top pressure ( $p_{ctop}^\ell$ ) are calculated by linearly interpolating the air temperature, and the three hydrometeor categories LWC, ice water content (IWC), snow water content (SWC) to the location of the WFJ every 5 hPa from the surface up to 100 hPa. The  $T_c^\ell$  above the WFJ is obtained as the weighted mean temperature using the total hydrometeor content ( $q_c$ ) at each pressure level as a weight. The total hydrometeor content  $q_c$  that is relevant for snow formation in clouds above the WFJ is defined here as the sum of the specific humidities from the three hydrometeor categories LWC, IWC, and SWC. Note that  $T_c^\ell$  is only an approximation of cloud formation temperature at the WFJ, albeit the best available, assuming that high concentrations of LWC, IWC, and SWC reflect cloudy regions, in which important snow formation occurs. The fourth hydrometeor category in the ERA5 data, rain water content (RWC), only appears during precipitation events from the end of March onwards. Since the influence of freezing rain is negligible for snow accumulation at WFJ, and because no direct condensation on falling rain drops can occur in the Integrated Forecasting System (IFS-CY41R2; ECMWF, 2016), RWC is not used. Although (supercooled) LWC is not very large in the considered winter and spring 2016/2017 period at the WFJ, it still occurs regularly even during winter snowfall events and is therefore taken into account in  $q_c$  for estimating  $T_c^\ell$ .

In addition, cloud top pressure was identified as the first pressure level starting from 100 hPa in steps of 5 hPa, where  $q_c$  was larger than  $50 \text{ mg kg}^{-1}$ . This threshold is chosen subjectively based on observed profiles and serves to avoid identifying spurious amounts of hydrometeors for example, in cirrus clouds as part of the precipitating clouds.

The moisture sources of the air parcels forming precipitation at the WFJ are diagnosed by applying a trajectory-based moisture source identification algorithm described in Sodemann et al. (2008). We calculated air parcel back-trajectories using LAGRANTO (Sprenger & Wernli, 2015a; Wernli, 1997) 10 days back in time using the three-dimensional wind fields of the hourly ERA5 reanalyzes. The back-trajectories are started every 3 hr in the period 1 November 2016–15 June 2017 from the WFJ. The starting points are vertically stacked between the surface (at about 850 hPa) and 300 hPa with a spacing of 50 hPa. The relevant environmental conditions at the moisture source (superscript s), such as the relative humidity with respect to surface (subscript s) temperature ( $h_s^s$ ) and the surface temperature ( $T_s^s$ ), are interpolated along the hourly trajectory positions for the subsequent calculation of Lagrangian moisture source conditions.



The moisture source conditions are calculated in the same way as in many previous studies (e.g., Pfahl and Wernli (2008); Aemisegger (2018); Thurnherr et al. (2021)). In short, a Lagrangian moisture budget is calculated for the air parcels, in which precipitation above the WFJ is formed, taking into account uptakes due to evaporation (increases in specific humidity) and losses (decreases in specific humidity) due to precipitation formation under way (see Sodemann et al. (2008) for more details on the method). The source conditions are obtained from the conditions at the time and location of the diagnosed uptakes along a given trajectory, weighted by the contribution of each uptake to the final precipitation. The contributions from the individual trajectories for a given time step are weighted according to their final specific humidity loss (i.e., their share in precipitation formation at the WFJ). Over the whole winter period, 95% of the precipitating moisture can be explained, the remaining 5% can be explained by moisture that has been taken up more than 10 days before arrival, or due to numerical uncertainties induced by the trajectory computation itself and the interpolation of the three-dimensional specific humidity field along it.

Five variables summarizing the moisture source (superscript  $s$ ), transport and cloud formation conditions locally at WFJ (superscript  $\ell$ ) are used and compared to the isotope samples of the snow profiles:

- *Moisture source*: relative humidity with respect to surface temperature  $h_s^s$  and surface temperature  $T_s^s$ .
- *Transport*: net air parcel cooling  $\Delta T = T_s^s - T_c^\ell$  due to ascent.
- *Cloud formation*: cloud formation temperature  $T_c^\ell$  and cloud top pressure  $p_{\text{ctop}}^\ell$  as a measure for vertical cloud extent.

These variables are all weighted by ERA5 surface precipitation at WFJ to compute the mean values within the time window corresponding to the individual snow samples in the profile. Additionally, the local air temperature at 2 m  $T_{2m}^\ell$  is used, for which the weighted mean over the individual sample time window is computed using new snow data derived from the corrected automatic snow height observations.

The meteorological conditions and dynamics of the snow cover in winter 2016–2017 are summarized in Figure 1. Thirty major snowfall events with more than 5 cm accumulation were recorded during the studied season, associated with either warm fronts (8), cold fronts (10), occluded fronts (7), low pressure systems (4), or an unidentified system (1, see Trachsel (2019) for more details). Two events with accumulation rates covering several of the sampled 6 cm snow profile sections (Figure 1c) were analyzed in more detail: a cold front (12 UTC on 12 January to 18 UTC on 15 January 2017) with 30 cm accumulation (yielding  $\sim 3$  samples after compaction), and a warm front (6 UTC on 30 January to 12 UTC on 2 February 2016) with 50 cm accumulation ( $\sim 5$  samples). The two studied events are separated by a prolonged period of 15 days with several events with only small amounts of new snow, during which the surface of the snow cover was exposed to potentially enhanced air-snow interactions.

### 3. Impact of Post-Depositional Dry and Wet Snow Metamorphism

By comparing the five isotope profiles as shown in Figure 3, we analyze the development of the isotopic signal deposited in the snow cover throughout the snow season. We thereby quantify and discuss the impact of dry and wet metamorphism on the isotope composition of the snow cover.

#### 3.1. Preservation of the Snow Isotope Signal During Cold Winter Despite Dry Metamorphism

The comparison of the first three sampled profiles (25 January, 22 February, and 21 March), during the cold part of the snow season at WFJ reveals an overall good preservation of the isotope signal at low temperatures with only a slight smoothing between the January and February profiles, and between the February and March profiles, in the range of around 1–2‰ in  $\delta^{18}\text{O}$  and 10–20‰ in  $\delta\text{D}$  (Figures 3a and 3b). The local maxima at SWEs of 10 and 20 cm and the minimum at 16 cm in the January profile are missing in the February and March profiles. Also the two local maxima at 29 and 33 cm SWE in the February  $\delta^{18}\text{O}$  and  $\delta\text{D}$  profile are smoothed out in the March profile. A plausible explanation for this smoothing are cycles of sublimation, vapor transport and resublimation during dry metamorphism within the snowpack. The directed vapor flux generated by the temperature gradient migrates from crystal to crystal without necessarily creating a continuous flow-through from the bottom to the top (Jafari et al., 2022; Yosida, 1955). The sublimated vapor molecules resublimates at a close-by ice crys-

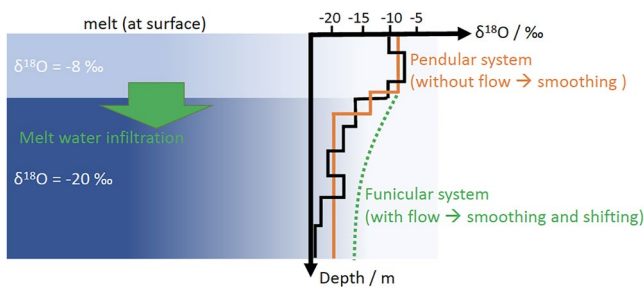


**Figure 4.** Change in isotopic profile during melt in pendular and funicular system in an idealized snowpack (homogeneously layered, 0°C isothermal). Original  $\delta^{18}\text{O}$  profile (black), smoothed  $\delta^{18}\text{O}$  profile due to non-percolating meltwater (orange), shifted  $\delta^{18}\text{O}$  profile due to meltwater percolation (green). At the transition from a pendular to a funicular system, the percolating water from the upper (idealized) layer begins to mix with the meltwater formed from a layer with different  $\delta^{18}\text{O}$ . The threshold for the transition between the pendular and the funicular states decreases from approximately 13%–18% liquid saturation for new snow to 7%–12% saturation for old, coarse-grained snow (Denoth, 1982).

tal (Pinzer et al., 2012; Sokratov & Maeno, 1997). Therefore, fractionation effects due to dry snow metamorphism are expected to have an impact on the scale of the pore size (Taylor et al., 2001). This leads to a local mixing of the water molecules resulting in a slightly smoothed profile of  $\delta^{18}\text{O}$  and  $\delta\text{D}$  from 1 month to the next without shifting the bulk signals of the snowpack toward more enriched values. Note that some degree of smoothing can also come from the sampling strategy. Due to compaction, the 6 cm samples cover increasing values of SWE in the lower part of the profile.

Vapor flux paths at the surface of the snow cover are different from those within the snow cover, because sublimated water molecules can escape into the atmosphere and are transported away by boundary layer turbulence. Assuming preferential volatilization of the lighter  $\text{H}_2^{16}\text{O}$  molecules, the proportion of heavy molecules in the remaining snow is thereby increased. Profile sections with potential influence of a net enrichment because of prolonged exposure to the atmosphere with low accumulation are marked in gray in Figure 1. The section around 29 cm is potentially affected by sublimation enrichment with an increase in the  $\delta^{18}\text{O}$  and  $\delta\text{D}$  signal along with a decrease in  $d$  observed in the February profile. The decrease in  $d$  is expected for net sublimation due to the preferential retention of  $\text{H}_2^{18}\text{O}$  in the snow cover due to a lower diffusivity in air compared to the deuterated water molecule (HDO). At SWE = 10 cm

a local minimum in  $d$  along with increasing  $\delta$  values toward the upper part of the exposed snow cover section indicate a possible sublimation influence. Above 11 cm the  $d$  strongly increases, which is unlikely related to sublimation and probably corresponds to the isotope signal of one (or several) of the light snowfall events in December or could be due to water vapor deposition during surface hoar formation (Figure 1a). Note that due to the many low-accumulation events in December the age reconstruction in this section of the profile is associated with larger uncertainties than in other parts of the snow cover. The increase in  $\delta^{18}\text{O}$  and  $\delta\text{D}$  potentially induced by sublimation is of  $\sim 2\text{--}3\text{‰}$  and  $\sim 10\text{--}12\text{‰}$  respectively, the decrease in  $d$  has an amplitude of  $3\text{‰}$ . These values correspond to previously observed snow surface isotope changes due to sublimation (Madsen et al., 2019; Moser & Stichler, 1975; Sokratov & Golubev, 2009; Steen-Larsen et al., 2014; Stichler et al., 2001).

To summarize, the  $\delta^{18}\text{O}$  ( $\delta\text{D}$ ) signal in the snow profiles sampled during the cold phase of the winter 2016/2017 shows variations of  $\sim 5\text{--}10\text{‰}$  ( $\sim 40\text{--}80\text{‰}$ ) between local maxima and minima in  $\delta^{18}\text{O}$  ( $\delta\text{D}$ ). Of these variations only minor smoothing effects of  $1\text{--}2\text{‰}$  ( $10\text{--}20\text{‰}$ ) can be attributed to post-depositional processes related to dry metamorphism in the snow cover.

### 3.2. Smoothing and Shifting of the Isotope Record in Spring Due To Wet Snow Metamorphism

As soon as rain- or melt-water is present in the snow cover, a complex system of recrystallization, mixing and fractionation processes is established. On the last two profile sampling dates in April and June, the snowpack was wet (Figure S3 in Supporting Information S1). A smoothing (reduction in amplitude) of  $2\text{‰}$  in  $\delta^{18}\text{O}$ ,  $18\text{‰}$  in  $\delta\text{D}$  and  $2\text{‰}$  in  $d$  is observed between the profiles of 17 April and 1 June (Figure 3). Additionally, an average shift of  $\sim +3\text{‰}$  in  $\delta^{18}\text{O}$ ,  $\sim +25\text{‰}$  in  $\delta\text{D}$  and  $\sim -2\text{‰}$  in  $d$  between these two spring profiles is apparent in Figure 3.

The pendular and funicular systems analogies from Denoth (1982) can explain the differences in the profiles from 17 April and 1 June compared to the other profiles sampled in winter (Figure 4). On both sampling days, the snow cover was already wet and therefore wet snow metamorphism was in progress. The SNOWPACK simulations show that from 21 March onwards, LWC inside the snow cover was increasing (Figure S3 in Supporting Information S1). From 4 April onwards the snowpack was completely wet, but the lowest layers were not yet completely saturated until May. Therefore, it can be assumed that the pendular system dominated in April: due to the moderate water input from the surface (begin of melt season), the impact of fractionation associated with wet snow metamorphism was limited to individual sections of the profiles (Figure 4, orange profile). More important smoothing in the April profile is thus observed compared to the March profile, due to wet snow metamorphism. The smoothing effect is especially strong in the upper part of the profiles ( $2\text{--}5\text{‰}$  in  $\delta^{18}\text{O}$ ,  $25\text{--}35\text{‰}$  in  $\delta\text{D}$  and  $2\text{--}4\text{‰}$  in  $d$ , Figure 3). Between April and June the liquid water concentration increased further (see Figure S3 in Supporting Information S1), accelerating wet snow metamorphism due to higher growth rates of the grains.

Moreover, transport of water from higher layers with a different  $\delta^{18}\text{O}$  compared to the lower layers became important. This leads to the heavy isotopic enrichment observed in  $\delta^{18}\text{O}$  and  $\delta\text{D}$  in June compared to the other profiles.

In summary, the enhanced infiltration of water can lead to an enrichment of the entire snow profile as can be observed in the profile of 1 June. Besides the clear shift, the  $\delta^{18}\text{O}$  and  $\delta\text{D}$  variability is still preserved to some extent (with the local maxima at 10 and 30 cm SWE and the local minima at 5 and 25 cm SWE in Figure 3). To find out whether the vertical variability pattern still reflects the variability of the original atmospheric signal more frequent sampling is required before and after the onset of melting. Additionally, meltwater should be collected during the melt season.

#### 4. Snow Isotope Links With Source, Transport, and Cloud Formation Processes

From the comparison of the different profiles in Figure 3, we derived estimates of the impact of different post-depositional processes in Section 3. Given the important alterations of the isotope signals in the snow due to wet snow metamorphism, we will concentrate the analysis on the atmospheric drivers of the isotope variability in the snow on the profiles of the cold winter season, and only include the sections that were not influenced by melt: 25 January, 22 February, and 21 March (lowest 52 cm SWE, due to the presence of liquid water in the upper part of the profile, see Figure S3 in Supporting Information S1).

The second order isotope parameter  $d$  has been shown in many recent studies of isotopes in water vapor and precipitation to preserve moisture source information, in particular about the relative humidity  $h_s^*$  at the moisture source (e.g., Aemisegger, 2018; Aemisegger et al., 2014; Pfahl & Wernli, 2008). The correlation between  $d$  and  $h_s^*$  ( $r(d, h_s^*)$ , Table 2) is particularly high for the first two profiles in the cold season. A lower value of  $r(d, h_s^*)$  is obtained for the March profile, most likely because of more important cumulative effects of dry snow metamorphism in the snow pack.

**Table 2**  
Pearson Correlations for the Dry Part of the Profiles Not Affected by Melting (Corresponding to Snow Water Equivalents up to 50 cm)

	Profile 1 25 January	Profile 2 22 February	Profile 3 21 March	Profile 4 17 April
Sample size	14	21	22	19
$r(\delta^{18}\text{O}, T_{2m}^{\ell})$	0.36	0.08	0.20	0.37
$r(\delta\text{D}, T_{2m}^{\ell})$	0.22	−0.08	0.04	0.25
$r(\delta^{18}\text{O}, T_c^{\ell})$	0.45	<b>0.59</b>	<b>0.55</b>	0.51
$r(\delta\text{D}, T_c^{\ell})$	0.39	0.52	0.52	0.51
$r(\delta^{18}\text{O}, T_s^s)$	0.28	0.08	0.15	0.20
$r(\delta\text{D}, T_s^s)$	0.15	−0.05	0.01	0.10
$r(\delta^{18}\text{O}, T_s^s - T_c^{\ell})$	−0.32	−0.50	−0.48	−0.40
$r(\delta\text{D}, T_s^s - T_c^{\ell})$	−0.34	−0.55	−0.53	−0.46
$r(\delta^{18}\text{O}, p_{\text{ctop}}^{\ell})$	0.04	<b>0.77</b>	<b>0.59</b>	0.49
$r(\delta\text{D}, p_{\text{ctop}}^{\ell})$	0.11	<b>0.74</b>	<b>0.63</b>	0.52
$r(d, h_s^*)$	−0.60	<b>−0.68</b>	−0.38	−0.26

*Note.* Correlations are shown between  $\delta^{18}\text{O}$ ,  $\delta\text{D}$ , and  $d$  in the snow profiles with the diagnosed meteorological conditions during snowfall. The local air temperature at 2 m is  $T_{2m}^{\ell}$ , the local cloud formation temperature  $T_c^{\ell}$ , the moisture source air temperature at 2 m  $T_s^s$ , the air mass total cooling from the source to cloud formation  $T_c^{\ell}$ , and the relative humidity with respect to sea surface temperature  $h_s^*$ . Bold values are shown if the  $p$ -value of the linear regression for a zero-slope null hypothesis is  $p < 0.01$  using a Wald Test with  $t$ -distribution of the test statistic.

The correlations between the surface temperature at the source and the  $\delta$  values is negligibly small in all profiles as are the correlations between the local near surface temperature and the  $\delta$  values. The influence of rain out processes during transport was analyzed using the net air mass cooling ( $T_s^s - T_c^{\ell}$ ), which has a notable but not significant influence on the  $\delta$  values in the profiles (Table 2). The local condensation temperature  $T_c^{\ell}$ , however shows consistently high correlations with both  $\delta^{18}\text{O}$  and  $\delta\text{D}$  in snow. Furthermore, the cloud top pressure  $p_{\text{ctop}}^{\ell}$ , which we use as a measure for vertical cloud extent shows strong relations with  $\delta^{18}\text{O}$  and  $\delta\text{D}$  for the February and March profiles. The fact that the correlations are all smaller in January is due to the higher uncertainties in the age reconstruction between 8 and 14 cm SWE reflected in the large discrepancies found between the SNOWPACK and  $\Delta\text{snow}$  reconstructions (see Figure 2).

For the cold part of the season without meltwater influence we thus find a strong relation between the local cloud properties ( $T_c^{\ell}$ ,  $p_{\text{ctop}}^{\ell}$ ) and the  $\delta$  signals, and between  $d$  and  $h_s^*$  at the moisture source. We observe high  $\delta$ -values in warm airmasses with comparatively shallow clouds and low  $\delta$ -values in cold airmasses with deeper clouds, reaching lower cloud top pressure (Figure 5a). Positive anomalies in snow  $d$  are observed in airmasses with water vapor originating from surface evaporation at low  $h_s^*$  (strong near-surface humidity gradients) and low  $T_s^s$  at the evaporation sites (Figure 5b). In the next section we investigate specific frontal passages and their associated imprints in snow isotope signals in winter.

#### 5. Isotope Signature of Frontal Passages

In the winter 2016–2017, cold precipitation events were associated with low  $\delta$  anomalies in the sampled snow profiles (local minima at SWEs of 8, 25 in Figures 6a and 6b). Precipitation formed in warm air masses led to several

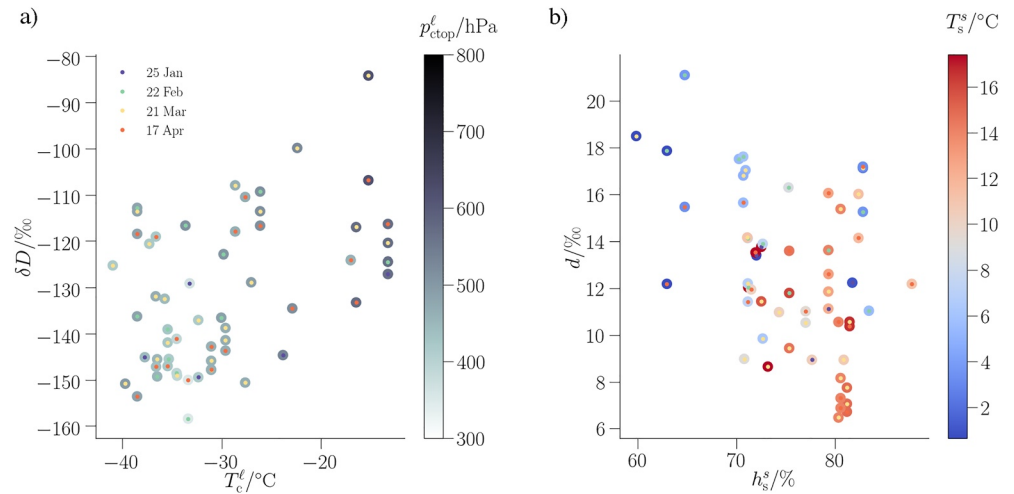


**Figure 5.** Isotope relations with cloud properties at Weissfluhjoch (a) and moisture source conditions (b) for the January–April profiles (for March and April only samples from the lowest 40 cm, unaffected by melt). In (a) the scatter plot shows  $T_c^\ell$  versus  $\delta D$  with colors showing  $p_{\text{ctop}}^\ell$  and in (b)  $h_s^s$  versus  $d$  with colors showing  $T_s^s$ .

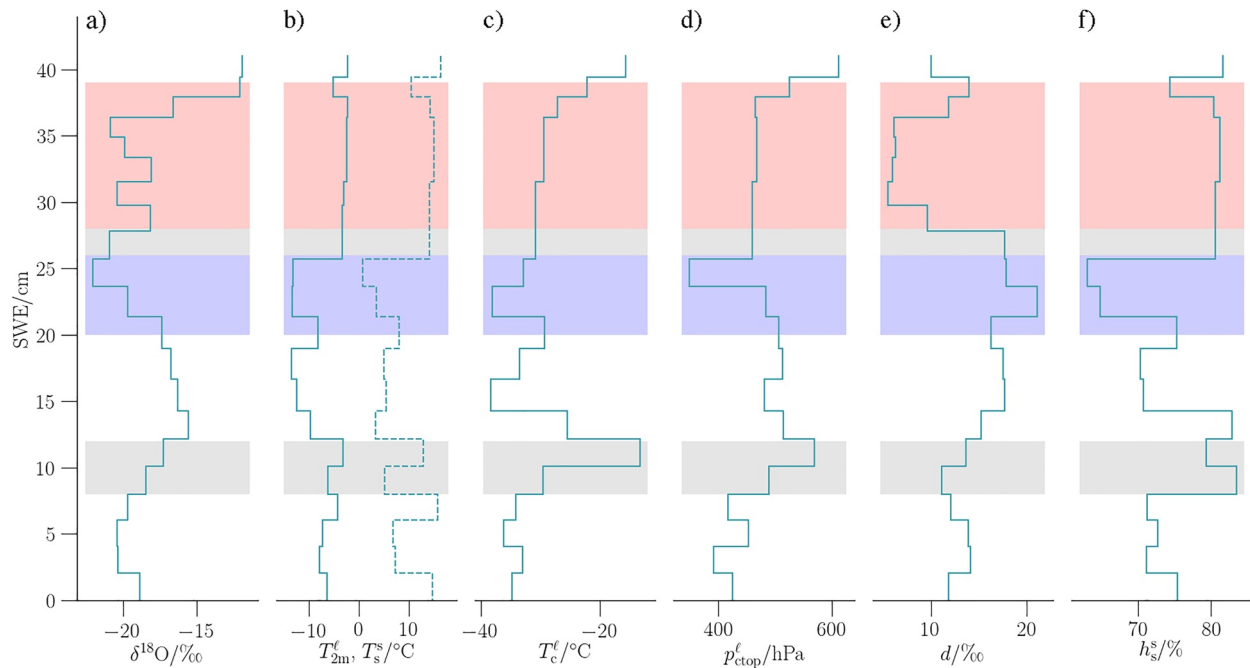


**Figure 6.** Profile 2 from 22 February 2017 with (a)  $\delta^{18}\text{O}$ , (b) local 2 m air temperature  $T_{2m}^\ell$  (solid line), and surface temperature at the moisture source  $T_s^s$  (dashed line), (c) cloud formation temperature  $T_c^\ell$ , (d) cloud top pressure ( $p_{\text{ctop}}^\ell$ ), (e)  $d$ , (f) relative humidity with respect to sea surface temperature at the moisture source  $h_s^s$ . Blue, red and gray shadings as in Figure 1.

local maxima in the  $\delta$  signals of the snow profiles (at SWEs of 12, 18, 38 in Figures 6a and 6b). The respective snowfall events are described in more detail in Trachsel (2019). Large variations of precipitation isotope signals during frontal passages have been previously discussed in the literature (e.g., Dansgaard, 1953; Dütsch et al., 2016; Thurnherr et al., 2021). Here we will focus on the archival of these isotope signals associated with frontal passages in the snow cover by analyzing two representative events in more detail, the cold front passage of 12–15 January 2017, which leads to the local  $\delta$  minimum at SWE = 24 cm; and the warm front passage between 30 January and 2 February, which leads to the local  $\delta$  maximum at SWE = 38 cm (Figure 6).



The cold front precipitation event at the WFJ between 12 and 15 January 2017 resulted from forced orographic uplift of cold air masses from the northern part of the North Atlantic (Figure 7a) with a large fraction of moisture sources located North of 45°N (Figure S4a in Supporting Information S1). The synoptic context of this event is characterized by an elongated upper-level trough reaching far South and favoring the advection of polar and subpolar airmasses over the North Atlantic toward Central Europe (Figure 7a). The northerly flow toward the Alps in the lower troposphere is established by an extratropical cyclone located over northeastern Europe and a meridionally elongated anticyclone in the eastern North Atlantic. The cold front arrived at WFJ at 6 UTC on 13 January (Figure 8a). Precipitation during this event formed in an environment of anomalously low atmospheric temperatures (Figure 8a, brown line shows  $T_c^\ell$ ).

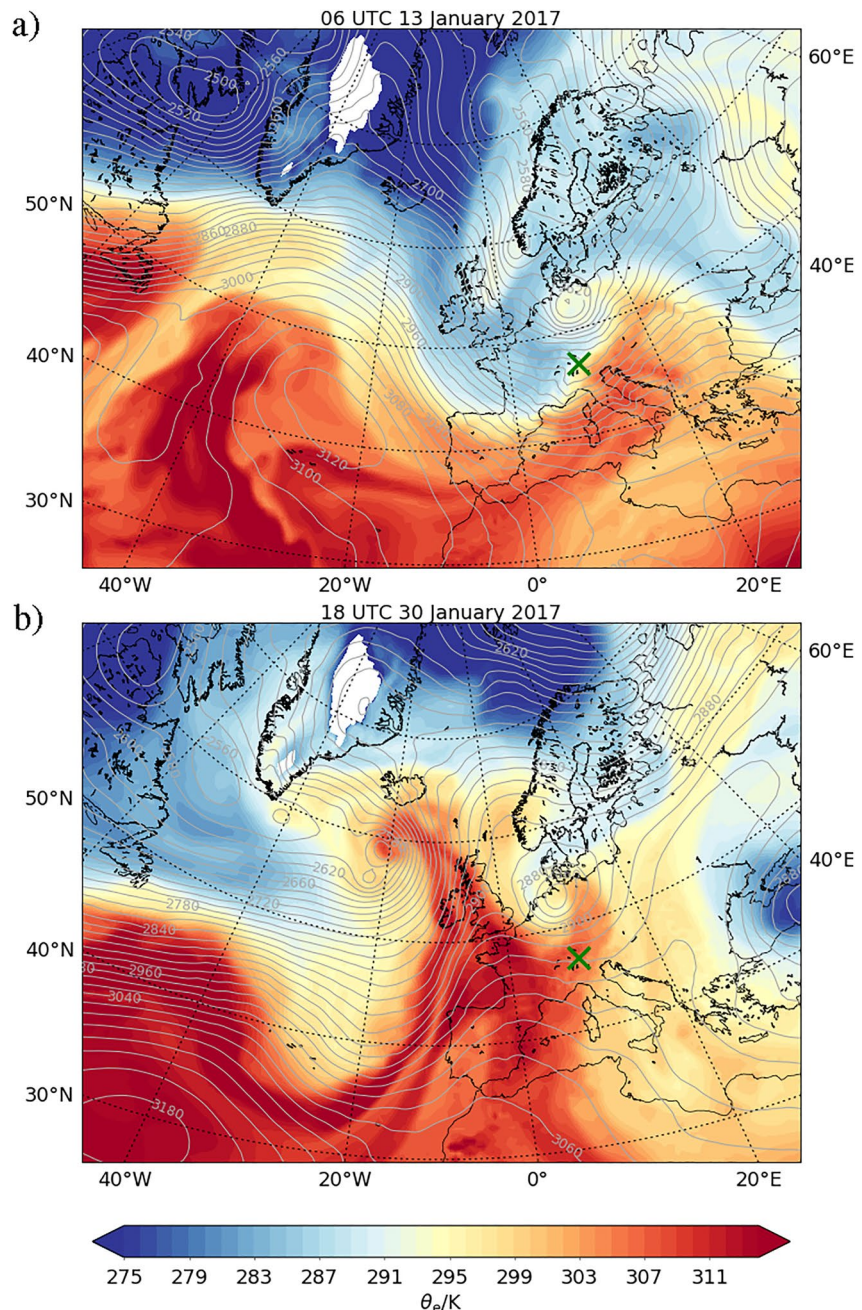


**Figure 7.** Large-scale weather situation for (a) the cold front, and (b) the warm front.  $\theta_e$  in filled contours and geopotential height at 700 hPa in gray contours. The position of the Weissfluhjoch is indicated by a green cross.



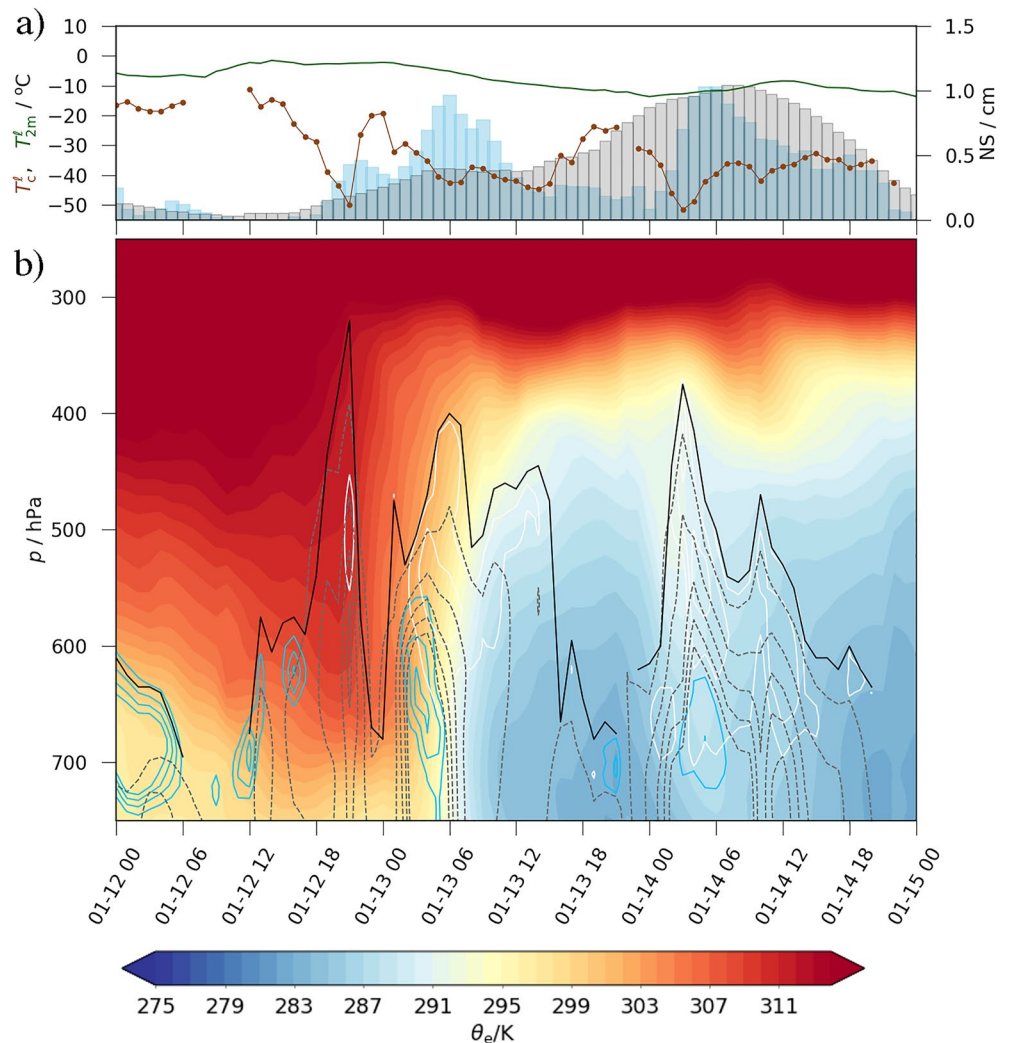


**Figure 8.** Temporal evolution of atmospheric conditions during the cold front passage. (a) New snow (NS) measured (gray bars) and in ERA5 (blue bars, right axis, assuming a new snow density of  $100 \text{ kg m}^{-3}$ ), measured 2 m temperature at the Weissfluhjoch in dark green and the diagnosed cloud formation temperature in connected brown dots (left axis). (b) Time-pressure plot for the two frontal passages with the equivalent potential temperature  $\theta_e$  in filled contours, hydrometeors in spacings of 50, 75, 100,  $125 \text{ mg kg}^{-1}$  for ice water content (white), snow water equivalent (additionally  $25 \text{ mg kg}^{-1}$ , gray dashed), liquid water content (light blue), cloud tops in black.

During the cold front passage, the  $\delta^{18}\text{O}$  and  $\delta\text{D}$  decreased by  $\sim 5\text{‰}$ , respectively by  $\sim 60\text{‰}$  (Figures 3a and 3b),  $T_c$  dropped from  $-18^{\circ}\text{C}$  to  $-40^{\circ}\text{C}$  within 2 days with some variations during periods with lower snowfall intensities (Figure 8a brown line). The drop in  $T_{2m}$  was more modest from  $-5^{\circ}\text{C}$  to  $-10^{\circ}\text{C}$  (Figure 8a green line). The temporal evolution of the vertical thermodynamic conditions and cloud structure above WFJ (Figure 8b) shows that the deepest clouds with the lowest  $T_c$  occurred during the most intense phases of precipitation in a locally unstable environment (around 21 UTC on 12 January, between 3 and 9 UTC on 13 January and between 3 and 6 UTC on 14 January). The timing of the ERA5 and the measured precipitation peak between 3 UTC and 18 UTC on 14 January deviates by only 3 hr (compare blue and gray bars in Figure 8a), however, the first two peaks in ERA5 (blue bars in Figure 8a) are overestimated compared to the observations (gray bars in Figure 8a).

The warm front precipitation event at the WFJ between 30 January and 2 February is associated with a strong zonal flow toward the Alps (Figure 7b) with warm and moist air transport from the subtropical and midlatitude North Atlantic (South of  $45^{\circ}\text{N}$ ) and/or from the Mediterranean (Figure S4 in Supporting Information S1, see also Trachsel (2019)). During the passage of the warm front at WFJ on 30 January, a deep surface cyclone moved

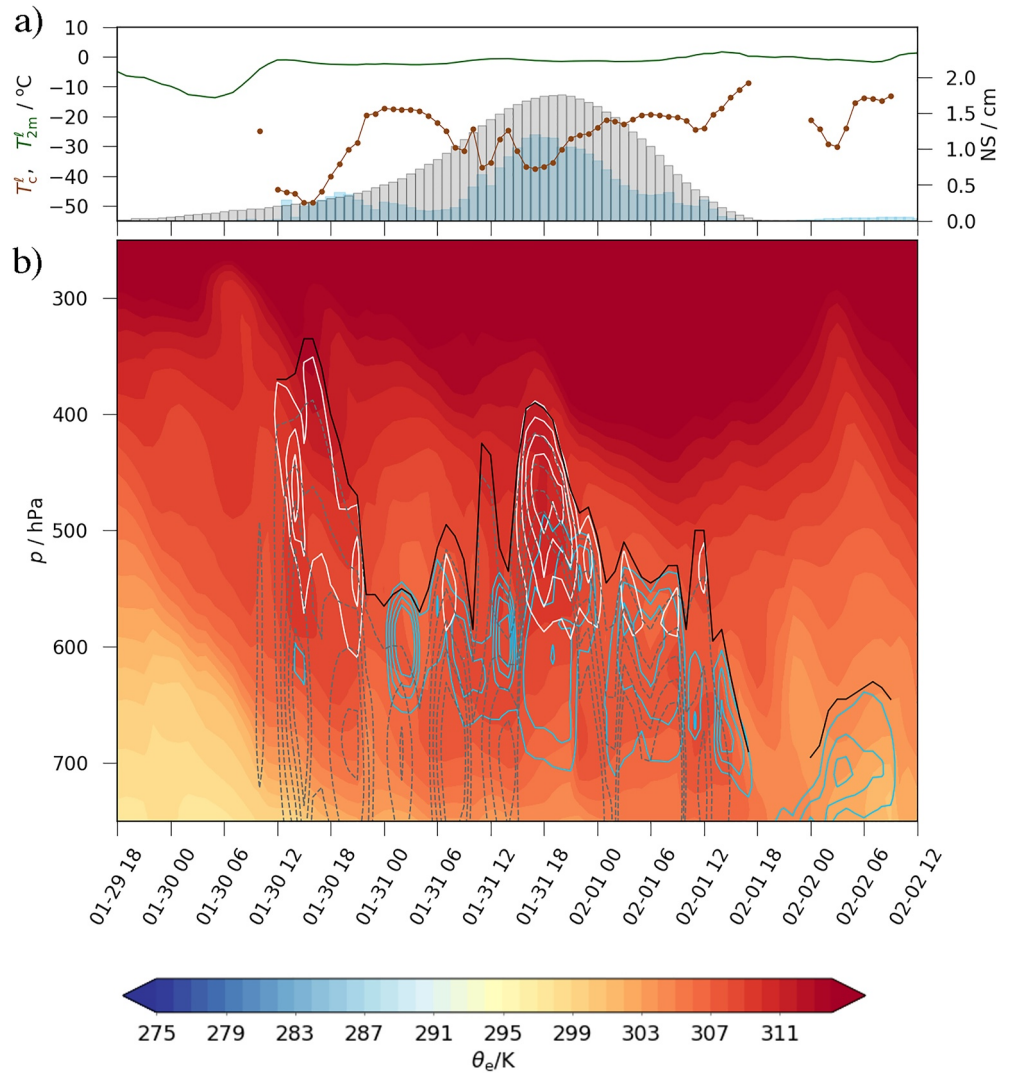


**Figure 9.** Temporal evolution of atmospheric conditions during the warm front. Panels and contours as in Figure 8.

northeastwards over the North Atlantic toward Norway and a second slightly weaker cyclone was located over northern Germany (Figure 6b). The latter cyclone's warm front arrived at WFJ at 15 UTC on 30 January, followed by a ridge building up from ~18 UTC on 31 January onwards.

During the warm front passage, the  $\delta^{18}\text{O}$  and  $\delta\text{D}$  increased by ~8‰, respectively by ~60‰ (Figures 3a and 3b),  $T_c^f$  increased from ~−40°C for the deep clouds at the leading edge of the warm front to −15°C in the shallower warm sector clouds after the precipitation peak within 2 days (Figures 6a and 9a). The increase in  $T_{2m}^f$  was more modest from −10°C to 0°C. The temporal evolution of the vertical thermodynamic conditions and cloud structure above WFJ (Figure 9b) shows that in contrast to the cold front passage, the deepest clouds with the lowest  $T_c^f$  occurred at the arrival of the warm front and not during the most intense phase of precipitation, during which the cloud is shallower and  $T_c^f$  about 10°C higher than during the peak intensity of the cold front precipitation event discussed above. The timing and intensity of the ERA5 precipitation peak between 12 UTC on 31 January and 00 UTC on 1 February agrees well with observations (compare blue and gray bars in Figure 9a).

The cold and warm front events analyzed here are both characterized by substantial intra-event variability in cloud vertical extent and condensation temperature. New snow sampled at high temporal resolution and additional information from local cloud and precipitation radars would provide insightful additional information and should be used in future campaigns. From the above two case analysis of one cold and one warm front passage,

it becomes clear that the main difference between the two precipitation events comes from the overall colder atmosphere during the cold front passage compared to the warm front, leading to lower  $T_c^\ell$  (compare  $T_c^\ell$  in blue and red sections of Figure 6c). The difference in isotope signals between cold and warm front passages is therefore induced primarily by the difference in large-scale temperature advection, while the vertical extent of the clouds and the cloud structure are most likely determining the short-term variability in the new snow's isotope composition.

## 6. Conclusions

In this study, we investigated the processes involved in the temporary archival of the atmospheric conditions leading to snowfall on the Weissfluhjoch (WFJ) in the Swiss Alps by combining snow profiles with a quantitative snow layer age reconstruction and atmospheric reanalysis data. The snow layer age reconstruction is based on two physically based snow models, the semi-empirical  $\Delta$ snow model and the thermodynamic SNOWPACK model, which are both driven by local snow height observations. To identify moisture sources of precipitating clouds at the WFJ, we used ERA5 reanalysis data, based on which we calculated three-dimensional back-trajectories. The ERA5 data also served to diagnose the cloud formation temperature and vertical cloud extent during frontal passages.

The isotope composition of five profiles sampled between January and June 2017 at approximately 1 month interval show that the isotope composition of the snow is conserved with a small impact of dry snow metamorphism during cold winter (variations of 1–2‰ in  $\delta^{18}\text{O}$ , 10–20‰ in  $\delta\text{D}$  and 3–5‰ in  $d$  between the overlapping profiles). Frontal passages are associated with distinct isotope signatures with an amplitude of  $\sim\pm 7\%$  in  $\delta^{18}\text{O}$ , and  $\sim\pm 60\%$  in  $\delta\text{D}$  due to changes in vertical cloud extent and cloud formation temperature. Strong links between  $\delta^{18}\text{O}$  (and  $\delta\text{D}$ ) with cloud formation temperature as well as mean air parcel cooling from the moisture source to cloud formation is found, while the correlation with local near-surface temperature is much weaker. A relation between precipitation isotopes and the vertical cloud extent (cloud-top pressure and temperature) has been found previously in low-latitude Asia at the monthly timescale (Cai & Tian, 2016). Here we investigated the role of cloud formation temperatures at the event timescale using vertical profiles through frontal clouds in the Alps.

Changes with an amplitude of  $\sim\pm 7\%$  in  $d$  are due to changes in moisture source conditions ( $h_s^s$  and  $T_s^s$ , see Aemisegger and Sjolte (2018) for a detailed discussion of the relative role of  $h_s^s$  and  $T_s^s$  for  $d$  at the moisture source). The strong relation between the  $d$  in snow and the conditions at the moisture source agrees well with the recent literature on the synoptic timescale variability of the  $d$  in precipitation (e.g., Aemisegger, 2018) and water vapor (Bonne et al., 2019; Pfahl & Wernli, 2008; Thurnherr et al., 2020).

As soon as the snow cover shows first signs of melting, exchange between the liquid, ice and vapor phase (wet snow metamorphism) leads to more important alterations of the isotope signature of the snow. The preferential removal of light isotopes during meltwater formation induces an overall enrichment of the remaining snow of  $\sim 3\%$  in  $\delta^{18}\text{O}$  and  $\sim 25\%$  in  $\delta\text{D}$ . Furthermore, the uncertainty in the snow sample's age reconstruction becomes very large due to partial melt from different layers and percolation of meltwater through the snow pack. Nevertheless, the vertical isotope variability structure is maintained, even though the absolute values have changed. The use of a melt-affected profile for reconstructing weather events seems therefore possible, even if it is associated with additional challenges due to the overall enrichment of the snow cover. In times of global warming and with melt-events occurring also in polar regions, this aspect becomes more and more relevant.

The two physically based models used for the snow layer age reconstruction agree within an uncertainty range of 1 and 2 cm snow water equivalent on the identified snowfall time of the sampled 6 cm snow layers. These age reconstructions are critically dependent on high-quality snow height measurements, with which they are driven. Automatic measurements with ultrasound sensors are affected by relatively large noise and can be associated with biases with respect to the manual measurements (see Supporting Information S1 and Ryan et al. (2021)). The largest discrepancies between the age reconstructions from  $\Delta$ snow and SNOWPACK are found in layers resulting from multiple low-accumulation events.

The synoptic-scale nature of the precipitation events leading to accumulation of snow at the WFJ warrants the use of the ERA5 reanalysis data set for characterizing the moisture sources, transport patterns and cloud formation conditions. This motivates future studies that include fresh snow sampling and collocated radar and satellite

observations to characterize the local cloud structure (condensation and deposition temperature, hydrometeor type, vertical extent, and sublimation below the cloud) in more detail. By combining a quantitative snow layer age reconstruction with the frontal cloud structure from reanalysis data and trajectory-based moisture source and transport diagnostics, this study allows to explicitly link isotope signals in the snow cover with relevant atmospheric processes. At locations without atmospheric observations, a reconstruction of atmospheric processes could thus be envisaged from snow profile sampling. The quality of precipitation forecasts from numerical weather prediction models is affected by important uncertainties associated with cloud and precipitation formation processes, in particular, in remote regions with complex topography and/or along frontal systems with embedded convection. Snow isotopes can therefore provide valuable additional constraints on cloud formation conditions that are complementary to traditional observations (Aemisegger et al., 2015).

High-resolution isotope-enabled simulations with a more detailed representation of topography and explicit treatment of embedded convective features within the frontal systems (e.g., Oertel et al., 2020) could provide more detailed insight into the precipitation producing cloud structure and condensation history. However, the correct timing and location of such small-scale features within the frontal systems in the simulations compared to observations is not guaranteed. Therefore a statistical analysis over the whole alpine range using simulations with a regional numerical model coupled to a multi-layer snow module is required. For such an approach, the present work has shown that the semi-empirical snow model  $\Delta\text{snow}$  provides a computationally efficient basis for high elevation regions in the cold season without melt. For more elaborate investigations on the impact of dry and wet snow metamorphism on the snow isotope profile, a fully coupled atmosphere-snow modeling system would be needed such as CRYOWRF (Sharma et al., 2021), which requires the implementation of isotope physics in a thermodynamic snow model such as SNOWPACK.

This study shows that synoptic-scale weather systems producing precipitation over the Alps leave a distinct imprint in the isotope composition of the snow cover, which reflects the vertical cloud structure and the moisture source conditions. The snow isotope signal is only marginally affected by post-depositional dry snow metamorphism, while wet snow-metamorphism is found to have a strong impact. These findings imply that the isotope signals from high-Alpine ice cores, if they are not strongly affected by melt, may provide information on the frequency of occurrence of frontal passages over the Alps. Major shifts in the upper-level jet stream and cyclone tracks likely leading to changes in moisture source regions and conditions (see, e.g., Aemisegger, 2018), could therefore be detectable in the isotope composition of Alpine ice.

## Data Availability Statement

The  $\delta^{18}\text{O}$  profile data (Avak, Trachsel, Edebeli, Brutsch, et al., 2019; Avak, Trachsel, Edebeli, Brutsch, et al., 2019) is available online (<https://www.ncdc.noaa.gov/paleo-search/study/26750>). The ERA5 reanalysis data (Hersbach et al., 2018) can be downloaded from the Copernicus Climate Service <https://climate.copernicus.eu/climate-reanalysis>. The Fortran code (Sprenger & Wernli, 2015b) for the trajectory calculations is available here <http://iacweb.ethz.ch/staff/sprenger/lagranto/download.html>. The R code for  $\Delta\text{snow}$  (Winkler et al., 2021a) can be downloaded here <https://cran.r-project.org/package=nixmass>. Information on SNOWPACK can be found at <https://www.slf.ch/de/services-und-produkte/snowpack.html>, and the code (Lehning et al., 2002b) is available at <https://gitlabext.wsl.ch/snow-models/snowpack>, last access 12 June 2021.

## Acknowledgments

The authors thankfully acknowledge helpful discussions with Fluregna Schindler, Pirmin Ebner, Johanna Spiegel-Pinzer, Henning Löwe, and Heini Wernli. Funding for JT and SA was provided by the Swiss National Science Foundation (SNSF) under Grant 155999. YS and ML acknowledge funding from the SNSF, Grant 179130. The authors thank MeteoSwiss and the ECMWF for the access to the ERA5 reanalysis data set. Sabina Brutsch is acknowledged for the stable water isotope analysis of the snow samples and her help during snow cover sampling. Michael Winkler and colleagues are acknowledged for providing their very well-documented delta-snow code.

## References

- Aemisegger, F. (2018). On the link between the North Atlantic storm track and precipitation deuterium excess in Reykjavik. *Atmospheric Science Letters*, 19(12), e865. <https://doi.org/10.1002/asl.865>
- Aemisegger, F., Pfahl, S., Sodemann, H., Lehner, I., Seneviratne, S. I., & Wernli, H. (2014). Deuterium excess as a proxy for continental moisture recycling and plant transpiration. *Atmospheric Chemistry and Physics*, 14(8), 4029–4054. <https://doi.org/10.5194/acp-14-4029-2014>
- Aemisegger, F., & Sjolte, J. (2018). A climatology of strong large-scale ocean evaporation events. Part II: Relevance for the deuterium excess signature of the evaporation flux. *Journal of Climate*, 31(18), 7313–7336. <https://doi.org/10.1175/JCLI-D-17-0592.1>
- Aemisegger, F., Spiegel, J. K., Pfahl, S., Sodemann, H., Eugster, W., & Wernli, H. (2015). Isotope meteorology of cold front passages: A case study combining observations and modeling. *Geophysical Research Letters*, 42(13), 5652–5660. <https://doi.org/10.1002/2015GL063988>
- Ala-Aho, P., Tetzlaff, D., McNamara, J. P., Laudon, H., & Soulsby, C. (2017). Using isotopes to constrain water flux and age estimates in snow-influenced catchments using the STARR (spatially distributed tracer-aided rainfall-runoff) model. *Hydrology and Earth System Sciences*, 21(10), 5089–5110. <https://doi.org/10.5194/hess-21-5089-2017>
- Albert, M., & Hardy, J. (1995). Ventilation experiments in a seasonal snow cover. In *Biogeochemistry of Seasonal Snow-Covered Proceedings of Symposium* (Vol. 228, pp. 41–49). IAHS.



- Albert, M., & Krajewski, G. (1998). A fast, physically based point snowmelt model for use in distributed applications. *Hydrological Processes*, 12(10–11), 1809–1824. [https://doi.org/10.1002/\(sici\)1099-1085\(199808/09\)12:10<1809::aid-hyp696>3.0.co;2-5](https://doi.org/10.1002/(sici)1099-1085(199808/09)12:10<1809::aid-hyp696>3.0.co;2-5)
- Avak, S. E., Trachsel, J. C., Edebeli, J., Brüttsch, S., Bartels-Rausch, T., Schneebeli, M., et al. (2019a). Melt-induced fractionation of major ions and trace elements in an alpine snowpack. *Journal of Geophysical Research: Earth Surface*, 124, 1647–1657. <https://doi.org/10.1029/2019JF005026>
- Avak, S. E., Trachsel, J. C., Edebeli, J., Brüttsch, S., Bartels-Rausch, T., Schneebeli, M., et al. (2019b). Weissfluhjoch, Swiss Alps 2017 snow-pit major ions and trace element data. [Dataset]. National Centers for Environmental Information, NESDIS, NOAA, U.S. Department of Commerce. <https://doi.org/10.25921/7nfh-1p81>
- Avanzi, F., Petrucci, G., Matzl, M., Schneebeli, M., & De Michele, C. (2017). Early formation of preferential flow in a homogeneous snowpack observed by micro-CT. *Water Resources Research*, 53(5), 3713–3729. <https://doi.org/10.1002/2016WR019502>
- Baltensperger, U., Schwikowski, M., Gäggeler, H. W., Jost, D. T., Beer, J., Siegenthaler, U., et al. (1993). Transfer of atmospheric constituents into an alpine snow field. *Atmospheric Environment*, 27(12), 1881–1890. [https://doi.org/10.1016/0960-1686\(93\)90293-8](https://doi.org/10.1016/0960-1686(93)90293-8)
- Bartelt, P., & Lehning, M. (2002). A physical snowpack model for the Swiss avalanche warning: Part I: Numerical model. *Cold Regions Science and Technology*, 35(3), 123–145. [https://doi.org/10.1016/S0165-232X\(02\)00074-5](https://doi.org/10.1016/S0165-232X(02)00074-5)
- Beria, H., Larsen, J. R., Ceperley, N. C., Michelon, A., Vennemann, T., & Schaeffli, B. (2018). Understanding snow hydrological processes through the lens of stable water isotopes. *WIREs Water*, 5(6), e1311. <https://doi.org/10.1002/wat2.1311>
- Bohleber, P., Wagenbach, D., Schöner, W., & Böhm, R. (2013). To what extent do water isotope records from low accumulation Alpine ice cores reproduce instrumental temperature series? *Tellus B: Chemical and Physical Meteorology*, 65(1), 20148. <https://doi.org/10.3402/tellusb.v65i0.20148>
- Bonne, J. L., Behrens, M., Meyer, H., Kipfstuhl, S., Rabe, B., Schönicke, L., et al. (2019). Resolving the controls of water vapour isotopes in the Atlantic sector. *Nature Communications*, 10(1), 1632. <https://doi.org/10.1038/s41467-019-09242-6>
- Brönnimann, S., Mariani, I., Schwikowski, M., Auchmann, R., & Eichler, A. (2013). Simulating the temperature and precipitation signal in an Alpine ice core. *Climate of the Past*, 9(4), 2013–2022. <https://doi.org/10.5194/cp-9-2013-2013>
- Brun, E. (1988). Investigation on wet-snow metamorphism in respect of liquid-water content. *Annals of Glaciology*, 13, 22–26. <https://doi.org/10.3189/S0260305500007576>
- C3S—Copernicus Climate Change Service. (2017). ERA5: Fifth generation of ECMWF atmospheric reanalyses of the global climate copernicus climate change service climate data store (CDS). Retrieved from <https://cds.climate.copernicus.eu>
- Cai, Z., & Tian, L. (2016). Atmospheric controls on seasonal and interannual variations in the precipitation isotope in the East Asian monsoon region. *Journal of Climate*, 29(4), 1339–1352. <https://doi.org/10.1175/JCLI-D-15-0363.1>
- Calonne, N., Richter, B., Löwe, H., Cetti, C., ter Schure, J., Van Herwijnen, A., et al. (2020). The RHOSA campaign: Multi-resolution monitoring of the seasonal evolution of the structure and mechanical stability of an Alpine snowpack. *The Cryosphere*, 14(6), 1829–1848. <https://doi.org/10.5194/tc-14-1829-2020>
- Casado, M., Landais, A., Picard, G., Münch, T., Laepple, T., Stenni, B., et al. (2018). Archival processes of the water stable isotope signal in East Antarctic ice cores. *The Cryosphere*, 12(5), 1745–1766. <https://doi.org/10.5194/tc-12-1745-2018>
- Colbeck, S. (1986). Statistics of coarsening in water-saturated snow. *Acta Metallurgica*, 34(3), 347–352. [https://doi.org/10.1016/0001-6160\(86\)90070-2](https://doi.org/10.1016/0001-6160(86)90070-2)
- Coplen, T. B. (2011). Guidelines and recommended terms for expression of stable-isotope-ratio and gas-ratio measurement results. *Rapid Communications in Mass Spectrometry*, 25(17), 2538–2560. <https://doi.org/10.1002/rcm.5129>
- Craig, H. (1961). Isotopic variations in meteoric waters. *Science*, 133(3465), 1702–1703. <https://doi.org/10.1126/science.133.3465.1702>
- Craig, H., & Gordon, L. (1964). Deuterium and oxygen-18 variations in the ocean and the marine atmosphere. In *Proceedings of the stable isotopes in oceanographic studies and paleotemperatures. Consiglio nazionale delle ricerche, Laboratorio di geologia nucleare*.
- Cuffey, K. M., Clow, G. D., Alley, R. B., Stuiver, M., Waddington, E. D., & Saltus, R. W. (1995). Large Arctic temperature change at the Wisconsin-Holocene glacial transition. *Science*, 270(5235), 455–458. <https://doi.org/10.1126/science.270.5235.455>
- Dansgaard, W. (1953). The abundance of  $O^{18}$  in atmospheric water and water vapour. *Tellus*, 5(4), 461–469. <https://doi.org/10.1111/j.2153-3490.1953.tb01076.x>
- Dansgaard, W. (1964). Stable isotopes in precipitation. *Tellus*, 16(4), 436–468. <https://doi.org/10.1111/j.2153-3490.1964.tb00181.x>
- Denoth, A. (1982). The pendular-funicular liquid transition and snow metamorphism. *Journal of Glaciology*, 28(99), 357–364. <https://doi.org/10.1017/S0022143000011692>
- Doorschot, J. J. J., Lehning, M., & Vrouwe, A. (2004). Field measurements of snow-drift threshold and mass fluxes, and related model simulations. *Boundary-Layer Meteorology*, 113(3), 347–368. <https://doi.org/10.1007/s10546-004-8659-z>
- Dütsch, M., Pfahli, S., & Sodemann, H. (2017). The impact of nonequilibrium and equilibrium fractionation on two different deuterium excess definitions. *Journal of Geophysical Research: Atmospheres*, 122, 12732–12746. <https://doi.org/10.1002/2017JD027085>
- Dütsch, M., Pfahli, S., & Wernli, H. (2016). Drivers of  $\delta^2H$  variations in an idealized extratropical cyclone. *Geophysical Research Letters*, 43(10), 5401–5408. <https://doi.org/10.1002/2016GL068600>
- Ebner, P. P., Steen-Larsen, H. C., Stenni, B., Schneebeli, M., & Steinfeld, A. (2017). Experimental observation of transient  $\delta^{18}O$  interaction between snow and advective airflow under various temperature gradient conditions. *The Cryosphere*, 11, 1733–1743. <https://doi.org/10.5194/tc-11-1733-2017>
- ECMWF. (2016). IFS Documentation, CY41R2 - Part IV: Physical processes. Retrieved from <https://www.ecmwf.int/node/16648>
- Eichler, A., Olivier, S., Henderson, K., Laube, A., Beer, J., Papina, T., et al. (2009). Temperature response in the Altai region lags solar forcing. *Geophysical Research Letters*, 36(1), L01808. <https://doi.org/10.1029/2008GL035930>
- Eichler, A., Schwikowski, M., Gäggeler, H., Furrer, V., Synal, H., Beer, J., et al. (2000). Glaciochemical dating of an ice core from upper Grenzgletscher (4200 m a.s.l.). *Journal of Glaciology*, 507–515(154), 46–515. <https://doi.org/10.3189/172756500781833098>
- Eichler, A., Schwikowski, M., & Gäggeler, H. W. (2001). Meltwater-induced relocation of chemical species in Alpine firn. *Tellus B: Chemical and Physical Meteorology*, 53(2), 192–203. <https://doi.org/10.3402/tellusb.v53i2.16575>
- Epstein, S., & Mayeda, T. (1953). Variation of  $O^{18}$  content of waters from natural sources. *Geochimica et Cosmochimica Acta*, 4(5), 213–224. [https://doi.org/10.1016/0016-7037\(53\)90051-9](https://doi.org/10.1016/0016-7037(53)90051-9)
- Gat, J. (1996). Oxygen and hydrogen isotopes in the hydrologic cycle. *Annual Review of Earth and Planetary Sciences*, 24(1), 225–262. <https://doi.org/10.1146/annurev.earth.24.1.225>
- Gkinis, V., Vinther, B. M., Popp, T. J., Quistgaard, T., Faber, A.-K., Holme, C. T., et al. (2021). A 120,000-year long climate record from a NW-Greenland deep ice core at ultra-high resolution. *Scientific Data*, 8(1), 141. <https://doi.org/10.1038/s41597-021-00916-9>
- Hersbach, H., Bell, B., Berrisford, P., Biavati, G., Horányi, A., Muñoz Sabater, J., et al. (2018). ERA5 hourly data on pressure levels from 1959 to present. [Dataset]. Copernicus Climate Change Service (C3S) Climate Data Store (CDS). Retrieved from <https://climate.copernicus.eu/climate-reanalysis>



- Hersbach, H., Bell, B., Berrisford, P., Hirahara, S., Horányi, A., Muñoz Sabater, J., et al. (2020). The ERA5 global reanalysis. *The Quarterly Journal of the Royal Meteorological Society*, 146(730), 1999–2049. <https://doi.org/10.1002/qj.3803>
- Hersbach, H., Bell, W., Berrisford, P., Horányi, A., Muñoz Sabater, J., Nicolas, J., et al. (2019). Global reanalysis: Goodbye ERA-interim, hello ERA5. *ECMWF Newsl.*, 159, 17–24. <https://doi.org/10.21957/vf291hehd7>
- IAEA. (2017). *Reference sheet for VSMOW2 and SLAP2 international measurement standards* (Tech. Rep.). International Atomic Energy Agency. Retrieved from [https://nucleus.iaea.org/sites/ReferenceMaterials/Shared/20Documents/ReferenceMaterials/StableIsotopes/VSMOW2/VSMOW2\\_SLAP2.pdf](https://nucleus.iaea.org/sites/ReferenceMaterials/Shared/20Documents/ReferenceMaterials/StableIsotopes/VSMOW2/VSMOW2_SLAP2.pdf)
- Jafari, M., Sharma, V., & Lehning, M. (2022). Convection of water vapour in snowpacks. *Journal of Fluid Mechanics*, 934, A38. <https://doi.org/10.1017/jfm.2021.1146>
- Johnsen, S. J., Dahl-Jensen, D., Dansgaard, W., & Gundestrup, N. (1995). Greenland palaeotemperatures derived from GRIP bore hole temperature and ice core isotope profiles. *Tellus*, 47(5), 624–629. <https://doi.org/10.1034/j.1600-0889.47.issue5.9.x>
- Jouzel, J. (2013). A brief history of ice core science over the last 50 yr. *Climate of the Past*, 9(6), 2525–2547. <https://doi.org/10.5194/cp-9-2525-2013>
- Jouzel, J., Alley, R. B., Cuffey, K. M., Dansgaard, W., P., G., Hoffmann, G., et al. (1997). Validity of the temperature reconstruction from water isotopes in ice cores. *Journal of Geophysical Research*, 102(C12), 26471–26487. <https://doi.org/10.1029/97JC01283>
- Laepfle, T., Werner, M., & Lohmann, G. (2011). Synchronicity of Antarctic temperatures and local solar insolation on orbital timescales. *Nature*, 471(7336), 91–94. <https://doi.org/10.1038/nature09825>
- Lee, J., Feng, X., Posmentier, E. S., Faiia, A. M., & Taylor, S. (2009). Stable isotopic exchange rate constant between snow and liquid water. *Chemical Geology*, 260(1–2), 57–62. <https://doi.org/10.1016/j.chemgeo.2008.11.023>
- Lehning, M., Bartelt, P., Brown, B., & Fierz, C. (2002). A physical snowpack model for the Swiss avalanche warning: Part III: Meteorological forcing, thin layer formation and evaluation. *Cold Regions Science and Technology*, 35(3), 169–184. [https://doi.org/10.1016/S0165-232X\(02\)00072-1](https://doi.org/10.1016/S0165-232X(02)00072-1)
- Lehning, M., Bartelt, P., Brown, B., Fierz, C., & Satyawali, P. (2002a). A physical snowpack model for the Swiss avalanche warning: Part II: Snow microstructure. *Cold Regions Science and Technology*, 35(3), 169–184. [https://doi.org/10.1016/S0165-232X\(02\)00072-1](https://doi.org/10.1016/S0165-232X(02)00072-1)
- Lehning, M., Bartelt, P., Brown, B., Fierz, C., & Satyawali, P. (2002b). Snowpack. [Software]. GitLab. <https://gitlabext.wsl.ch/snow-models/snowpack>
- Lehning, M., Lowe, H., Ryser, M., & Raderschall, N. (2008). Inhomogeneous precipitation distribution and snow transport in steep terrain. *Water Resources Research*, 44(7), W07404. <https://doi.org/10.1029/2007wr006545>
- Madsen, M. V., Steen-Larsen, H. C., Hörhold, M., Box, J., Berben, S. M. P., Capron, E., et al. (2019). Evidence of isotopic fractionation during vapor exchange between the atmosphere and the snow surface in Greenland. *Journal of Geophysical Research: Atmospheres*, 124(6), 2932–2945. <https://doi.org/10.1029/2018JD029619>
- Mariani, I., Eichler, A., Jenk, T. M., Brönnimann, S., Auchmann, R., Leuenberger, M. C., & Schwikowski, M. (2014). Temperature and precipitation signal in two Alpine ice cores over the period 1961–2001. *Climate of the Past*, 10(3), 1093–1108. <https://doi.org/10.5194/cp-10-1093-2014>
- Marty, C., & Meister, R. (2012). Long-term snow and weather observations at Weissfluhjoch and its relation to other high-altitude observatories in the Alps. *Theoretical and Applied Climatology*, 110(4), 573–583. <https://doi.org/10.1007/s00704-012-0584-3>
- Masson-Delmotte, V., Hou, S., Ekaykin, A., Jouzel, J., Aristarain, A., Bernardo, R., et al. (2008). A review of Antarctic surface snow isotopic composition: Observations, atmospheric circulation, and isotopic modeling. *Journal of Climate*, 21(13), 3359–3387. <https://doi.org/10.1175/2007JCLI2139.1>
- Masson-Delmotte, V., Jouzel, J., Landais, A., Stievenard, M., Johnsen, S. J., White, J. W. C., et al. (2005). GRIP deuterium excess reveals rapid and orbital-scale changes in Greenland moisture origin. *Science*, 309(5731), 118–121. <https://doi.org/10.1126/science.1108575>
- Moser, H., & Stiehler, W. (1975). Deuterium and oxygen-18 contents as an index of the properties of snow covers. In *Proceedings of the Grindelwald Symposium, April 1974 (Grindelwald)*, *Snow Mechanics* (p. 442). Retrieved from [http://hydrologie.org/redbooks/a114/iahs\\_114\\_0122.pdf](http://hydrologie.org/redbooks/a114/iahs_114_0122.pdf)
- Oertel, A., Boettcher, M., Joos, H., Sprenger, M., & Wernli, H. (2020). Potential vorticity structure of embedded convection in a warm conveyor belt and its relevance for large-scale dynamics. *Weather and Climate Dynamics*, 1, 127–153. <https://doi.org/10.5194/wcd-1-127-2020>
- Pfahli, S., & Wernli, H. (2008). Air parcel trajectory analysis of stable isotopes in water vapor in the eastern Mediterranean. *Journal of Geophysical Research*, 113(D20), D20104. <https://doi.org/10.1029/2008JD009839>
- Pinzer, B. R., Schneebeli, M., & Kaempfer, T. U. (2012). Vapor flux and recrystallization during dry snow metamorphism under a steady temperature gradient as observed by time-lapse microtomography. *The Cryosphere*, 6(5), 1141–1155. <https://doi.org/10.5194/tc-6-1141-2012>
- Raymond, C. F., & Tusima, K. (1979). Grain coarsening of water-saturated snow. *Journal of Glaciology*, 22(86), 83–105. <https://doi.org/10.3189/S002214300014076>
- Rüdisühli, S., Sprenger, M., Leutwyler, D., Schär, C., & Wernli, H. (2020). Attribution of precipitation to cyclones and fronts over Europe in a kilometer-scale regional climate simulation. *Weather and Climate Dynamics*, 1(2), 675–699. <https://doi.org/10.5194/wcd-1-675-2020>
- Ryan, W. A., Doesken, N. J., & Fassnacht, S. R. (2021). Evaluation of ultrasonic snow depth sensors for U.S. snow measurements. *Journal of Atmospheric and Oceanic Technology*, 25(5), 667–684. <https://doi.org/10.1175/2007JTECHA947.1>
- Schmucki, E., Marty, C., Fierz, C., & Lehning, M. (2014). Evaluation of modelled snow depth and snow water equivalent at three contrasting sites in Switzerland using snowpack simulations driven by different meteorological data input. *Cold Regions Science and Technology*, 99, 27–37. <https://doi.org/10.1016/j.coldregions.2013.12.004>
- Schwikowski, M. (1997). Analytical chemistry in High-Alpine environmental research. *CHIMIA International Journal for Chemistry*, 51(10), 786–789. <https://doi.org/10.2533/chimia.1997.786>
- Sharma, V., Gerber, F., & Lehning, M. (2021). Introducing cryowrf v1.0: Multiscale atmospheric flow simulations with advanced snow cover modelling. *Geoscientific Model Development Discussions*, 2021, 1–46. <https://doi.org/10.5194/gmd-2021-231>
- Sime, L. C., Marshall, G. J., Mulvaney, R., & Thomas, E. R. (2009). Interpreting temperature information from ice cores along the Antarctic Peninsula: ERA40 analysis. *Geophysical Research Letters*, 36(18), L18801. <https://doi.org/10.1029/2009GL038982>
- Sodemann, H., Schwierz, C., & Wernli, H. (2008). Interannual variability of Greenland winter precipitation sources: Lagrangian moisture diagnostic and North Atlantic oscillation influence. *Journal of Geophysical Research*, 113(D3), D03107. <https://doi.org/10.1029/2007JD008503>
- Sokratov, S. A., & Golubev, V. N. (2009). Snow isotopic content change by sublimation. *Journal of Glaciology*, 55(193), 823–828. <https://doi.org/10.3189/002214309790152456>
- Sokratov, S. A., & Maeno, N. (1997). Heat and mass transport in snow under a temperature gradient. In I. Izumi, T. Nakamura, & R. L. Sack (Eds.), *Snow engineering: Recent advances (Proceedings of the Third International Conference on Snow Engineering, Sendai, Japan, May 1996)* (pp. 49–54). <https://doi.org/10.13140/2.1.3331.9206>
- Sprenger, M., & Wernli, H. (2015a). The LAGRANTO Lagrangian analysis tool—Version 2.0. *Geosci. Geoscientific Model Development*, 8, 2569–2586. <https://doi.org/10.5194/gmd-8-2569-2015>

- Sprenger, M., & Wernli, H. (2015b). LAGRANTO, the Lagrangian analysis tool. [Software]. ETH Zürich. Retrieved from <https://iacweb.ethz.ch/staff/sprenger/lagranto/>
- Steen-Larsen, H., Masson-Delmotte, V., Hirabayashi, M., Winkler, R., Satow, K., Prié, F., et al. (2014). What controls the isotopic composition of Greenland surface snow. *Climate of the Past*, 10(1), 377–392. <https://doi.org/10.5194/cp-10-377-2014>
- Steig, E. J., Ding, Q., White, J. W. C., Küttel, M., Rupper, S. B., Neumann, T. A., et al. (2013). Recent climate and ice-sheet changes in West Antarctica compared with the past 2,000 years. *Nature Geoscience*, 6(5), 372–375. <https://doi.org/10.1038/ngeo1778>
- Stichler, W., Schotterer, U., Fröhlich, K., Ginot, P., Kull, C., Gäggeler, H., & Pouyaud, B. (2001). Influence of sublimation on stable isotope records recovered from high-altitude glaciers in the tropical Andes. *Journal of Geophysical Research*, 106(D19), 22613–22620. <https://doi.org/10.1029/2001JD900179>
- Sturm, C., Zhang, Q., & Noone, D. (2010). An introduction to stable water isotopes in climate models: Benefits of forward proxy modelling for paleoclimatology. *Climate of the Past*, 6(1), 115–129. <https://doi.org/10.5194/cp-6-115-2010>
- Sturm, M., & Benson, C. (1997). Vapor transport, grain growth and depth-hoar development in the subarctic snow. *Journal of Glaciology*, 43(143), 42–59. <https://doi.org/10.3189/S0022143000002793>
- Taylor, S., Feng, X., Kirchner, J. W., Osterhuber, R., Klaue, B., & Renshaw, C. E. (2001). Isotopic evolution of a seasonal snowpack and its melt. *Water Resources Research*, 37(3), 759–769. <https://doi.org/10.1029/2000WR900341>
- Thompson, L. G., Mosley-Thompson, E., Davis, M. E., Zagorodnov, V. S., Howat, I. M., Mikhalenko, V. N., & Lin, P.-N. (2013). Annually resolved ice core records of tropical climate variability over the past 1,800 years. *Science*, 340(6135), 945–950. <https://doi.org/10.1126/science.1234210>
- Thurnherr, I., Hartmuth, K., Jansing, L., Gehring, J., Boettcher, M., Gorodetskaya, I., et al. (2021). The role of air–sea fluxes for the water vapour isotope signals in the cold and warm sectors of extratropical cyclones over the Southern Ocean. *Weather and Climate Dynamics*, 2, 331–357. <https://doi.org/10.5194/wcd-2-331-2021>
- Thurnherr, I., Kozachek, A., Graf, P., Weng, Y., Bolshiyarov, D., Landwehr, S., et al. (2020). Meridional and vertical variations of the water vapour isotopic composition in the marine boundary layer over the Atlantic and Southern Ocean. *Atmospheric Chemistry and Physics*, 20(9), 5811–5835. <https://doi.org/10.5194/acp-20-5811-2020>
- Trachsel, J. (2019). *Microscale distribution of environmental proxies in snow* (Doctoral dissertation), ETH Zuerich. <https://doi.org/10.3929/ethz-b-000387457>
- Walter, B., Horender, S., Gromke, C., & Lehning, M. (2013). Measurements of the pore-scale water flow through snow using fluorescent particle tracking velocimetry. *Water Resources Research*, 49(11), 7448–7456. <https://doi.org/10.1002/2013wr013960>
- Weng, Y., Johannessen, A., & Sodemann, H. (2021). High-resolution stable isotope signature of a land-falling atmospheric river in southern Norway. *Weather and Climate Dynamics*, 2(3), 713–737. <https://doi.org/10.5194/wcd-2-713-2021>
- Werner, M., Mikolajewicz, U., Heimann, M., & Hoffmann, G. (2000). Borehole versus isotope temperatures on Greenland: Seasonality does matter. *Geophysical Research Letters*, 27(5), 723–726. <https://doi.org/10.1029/1999GL006075>
- Wernli, H. (1997). A Lagrangian-based analysis of extratropical cyclones. II: A detailed case study. *Quarterly Journal of the Royal Meteorological Society*, 123(542), 1677–1706. <https://doi.org/10.1002/qj.49712354211>
- Wever, N., Fierz, C., Mitterer, C., Hirashima, H., & Lehning, M. (2014). Solving Richards Equation for snow improves snowpack meltwater runoff estimations in detailed multi-layer snowpack model. *The Cryosphere*, 8(1), 257–274. <https://doi.org/10.5194/tc-8-257-2014>
- Winkler, M., Schellander, H., & Gruber, S. (2021a). nixmass: Snow water equivalent modeling with the “delta.snow” model and empirical regression models. [Software]. Rdrr.io. Retrieved from <https://rdrr.io/cran/nixmass/man/>
- Winkler, M., Schellander, H., & Gruber, S. (2021b). Snow water equivalents exclusively from snow depths and their temporal changes: The Δsnow model. *Hydrology and Earth System Sciences*, 25(3), 1165–1187. <https://doi.org/10.5194/hess-25-1165-2021>
- Yosida, Z. (1955). Physical studies on deposited snow. Retrieved from <http://hdl.handle.net/2115/20216>